International Communications in Heat and Mass Transfer 159 (2024) 108033

Contents lists available at ScienceDirect

International Communications in Heat and Mass Transfer

journal homepage: www.elsevier.com/locate/ichmt

The application of thermomechanically coupled phase-field models in electronic packaging interconnect structures

Yanpeng Gong [a,b], Yuguo Kou [a], Qiang Yue [b,*], Xiaoying Zhuang [b,c,*], Fei Qin [a], Qiao Wang [d], Timon Rabczuk [e]

[a] Institute of Electronics Packaging Technology and Reliability, Department of Mechanics, Beijing University of Technology, Beijing 100124, China
[b] Chair of Computational Science and Simulation Technology, Institute of Photonics, Department of Mathematics and Physics, Leibniz University Hannover, 30167 Hannover, Germany
[c] Department of Geotechnical Engineering, College of Civil Engineering, Tongji University, Shanghai 200092, China
[d] State Key Laboratory of Water Resources Engineering and Management, Wuhan University, Wuhan, Hubei 430072, China
[e] Institute of Structural Mechanics, Bauhaus University Weimar, 99423 Weimar, Germany

ARTICLE INFO

Keywords:
Electronic packaging interconnect structures
Phase-field model
Thermomechanical coupling problems
Crack initiation and propagation

ABSTRACT

To achieve high-density, high-reliability integrated packaging interconnects, 3D packaging technology has become a focus of current research, where Through-Silicon Via (TSV) and Through-Glass Via (TGV) technologies are key interconnect technologies. However, in TSV and TGV structures, the mismatch in thermal expansion coefficients among various materials and the complexity of the interconnect structures can lead to significant thermal stress during production and use, severely affecting device performance and reliability. In this study, a thermomechanically coupled phase-field model that considers mixed-mode fracture is proposed to study the mechanical performance and fracture behavior of interconnect structures. The approach to studying coupled thermo-mechanical-damage models can indeed be divided into two parts, focusing first on microstructure generation using Voronoi polygons and second on conducting phase field simulations to analyze mechanical and fracture behaviors. The framework was applied to model the fracture of interconnect structures under thermal cyclic conditions, demonstrating the formation of distinctive crack patterns and complex crack networks. The cracking behaviors observed in the experiments and simulations are remarkably similar to each other. This research provides an efficient and reliable simulation method for enhancing the reliability of interconnect structures in 3D packaging technology.

1. Introduction

Since Moore's Law was proposed in 1965, it has continuously driven the development of integrated circuit technology towards miniaturization [1,2]. However, at the current stage, the scaling of transistors and the limitations of leakage currents lead to the failure of Moore's Law, presenting an insurmountable limit [3]. Three-dimensional (3D) packaging technologies are currently seen as a promising avenue for extending Moore's Law [4]. Within this realm, the interposer integration approach, leveraging Through-Silicon Vias (TSVs), is key to advanced system integration, facilitating the high-density 3D integration of numerous chips [5,6]. TSV technology allows for vertical connections between chips, efficiently minimizing the space required for interconnects and enhancing interconnect density. In TSV structures, the difference in thermal expansion coefficients between copper and silicon is significant. This thermal mismatch between materials can lead to thermal stress, causing interface delamination and the protrusion of filled copper in TSV structures. These issues limit the application of TSV interconnect structures in microsystems [7]. As a semiconductor interconnect structure, TSV technology necessitates the deposition of dielectric layers, which subsequently increases production costs. Moreover, silicon, being the semiconductor material in use, exhibits a relatively high loss tangent value. This characteristic significantly contributes to conductive and dielectric losses within the silicon substrate, adversely affecting the signal integrity of the TSV structure. Glass, with its adjustable coefficient of thermal expansion (CTE), excellent

---

* Corresponding authors at: Chair of Computational Science and Simulation Technology, Institute of Photonics, Department of Mathematics and Physics, Leibniz University Hannover, 30167 Hannover, Germany.

E-mail addresses: yanpeng.gong@bjut.edu.cn (Y. Gong), qiangyue@iop.uni-hannover.de (Q. Yue), zhuang@iop.uni-hannover.de (X. Zhuang).

https://doi.org/10.1016/j.icheatmasstransfer.2024.108033

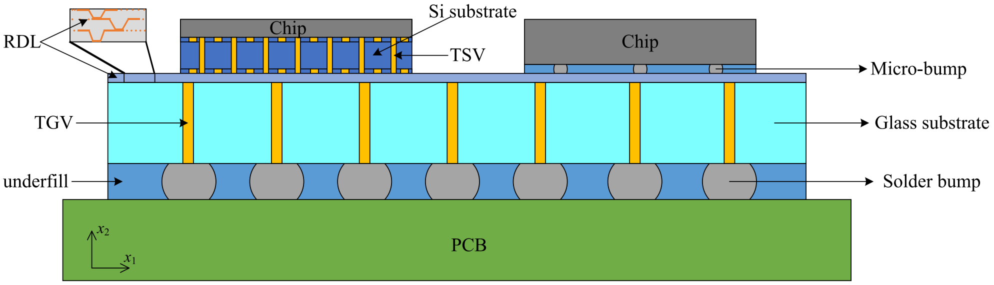

Fig. 1. Schematic diagram of system-level packaging based on a glass interposer.

surface flatness, high resistivity, and low cost, has become an attractive interposer material. The emergence of Through Glass Vias (TGV) provides another option for advanced manufacturing and packaging. As illustrated in Fig. 1, there's a schematic representation of a system-level packaging that utilizes a glass interposer. Similarly to TSV structures, the formation of metallized TGVs introduces thermal-mechanical challenges, due to the CTE mismatch between the glass substrate and the metal fill. The difference in CTE leads to high stress, resulting in various failure modes for TGVs, such as cracks in the glass substrate and delamination at the glass-Cu interface, among other destructive behaviors.

Researchers have spent many years investigating TSV structures and their reliability issues through experimental schemes. Okoro et al. investigated the reliability of TSV daisy chains under thermal cycling conditions and discovered that as the number of thermal cycles increased, cracking and voids occurred in the sidewall interconnect structures of TSVs [8]. Chen et al. studied the impact of different annealing rates on the protrusion of TSV-Cu [9]. They annealed TSV-Cu at 400 °C with heating rates of 0.1 °C/min, 1 °C/min, and 10 °C/min, respectively. After annealing, the protrusion morphologies exhibited characteristics of bulging at the edges, center, or overall, with the protrusion heights ranging between 0.4–0.7 μm. Additionally, as the heating rate increased, the protrusion height first increased and then decreased. In the literature [10], two different grain sizes of copper fill were used to study the impact of the microstructure of the filled Cu on the protrusion and mechanical properties of TSVs. It was found that the grain size of Cu has a direct correlation with the mechanical properties of TSVs. The results showed that the grain size of the filled Cu decreased after annealing, and this reduction in grain size can effectively reduce protrusion damage, thereby enhancing the reliability of TSVs. A comparatively recent development in the literature is the move to TGV analysis. The study in reference [11] investigated the impact of electroplating copper rings of different thicknesses inside TGV holes on structural cracking. The results indicated that the threshold thickness for the copper rings is 12 μm, meaning that when the thickness of the copper rings is less than 12 μm, no microcracks were observed, defining this as the crack-free copper ring thickness region. The studies mentioned above primarily caused failures in interconnect structures through cyclic thermo-mechanical reliability tests, with a focus on identifying and observing failure points. However, experimental research faces certain limitations, mainly because of lengthy experimental cycles, significant costs, and the reality that typically, only simpler interconnect structures can be prepared for testing. This approach often falls short of providing a comprehensive understanding of the failure mechanisms.

Numerical simulation offers a cost-effective solution capable of applying various loads and boundary conditions, enabling the acquisition of stress and displacement data across different regions and times. Its substantial value lies in monitoring, predicting effects, and optimizing structures, making it an effective complement and extension to experimental approaches. In reference [12], the authors investigated the steady-state energy release rate expressions for pre-embedded cracks at the Cu/Si interface in TSVs using a finite element method (FEM) based on fracture mechanics. They analyzed the impact of crack depth, TSV size, and filler materials on the energy release rate of interface cracks. DEMIR and collaborators [13,14] utilized finite element simulation to analyze the thermo-mechanical stress and strain in TGVs of different structures. Zhao and collaborators [15] investigated the evolution of thermal stress under different geometric and material parameters during the annealing process of TGVs. They conducted a numerical study based on a finite element model to analyze the stress distribution in TGV-Cu of different thicknesses. Such numerical simulation work primarily involve creating finite element models to calculate the stress and strain at critical locations within TGV/TSV models, using these metrics to analyze failure in the TGV/TSV models. However, due to the complex mechanical and thermal loads that interconnect structures must endure during manufacturing and use, various forms of failure, such as interface delamination and structural cracking, frequently occur. Merely relying on the aforementioned numerical simulation scheme is insufficient to obtain detailed information about the damage state, failure modes, and crack initiation locations of the structures. Therefore, there's a pressing requirement for a numerical simulation methodology capable of examining the real damage in interconnect structures. This would enable an investigation into preventing crack formation within the structure or exploring how cracks continue to evolve after their formation.

The phase-field method (PFM) stands out as a promising technique for pinpointing failure locations and understanding the modes of failure in interconnect structures subjected to mechanical and thermal stresses [16]. It adeptly handles mixed-mode fractures, enabling precise calculations of mechanical behaviors and the progression of cracks, including interface cracking in TSVs and substrate cracking within the glass matrix of TGVs. The most prominent advantage of the phase-field model lies in its use of the diffuse approach to continuous variables around the crack, eliminating the need for separate treatment of the crack surface and avoiding the crack tip singularity problem commonly found in discontinuous interface methods. Furthermore, the diffusion process transforms material damage into a field variable, enabling the direct determination of material failure states and crack patterns through the solution of control equations. With its advantages, the phase-field method has garnered significant attention from the research community and has been widely applied to various coupled damage scenarios [17], including thermo-mechanical coupling damage [16,18,19], thermoelastic coupling damage [20], chemo-mechanical coupling damage [21], chemo-mechanical-thermal coupling damage [22], electro-mechanical coupling damage [23], hydro-chemo-mechanical coupling damage [24], and hydro-poromechanical coupling damage [25], among others. In [26], Li and colleagues develop a phase-field approach to simulate hydrothermally induced crack extension in hot poroelastic media. In [27], the authors present the phase-field fracture model, detailing fatigue theory and its numerical implementation. In [16], Badnava and co-authors introduced an h-adaptive thermo-mechanical phase field model for fracture. They employed a predictor-corrector mesh refinement strategy within their mesh refinement algorithm, specifically tailored for applications in thermo-mechanical fracture models. The paper presents several thermo-mechanical examples to demonstrate the

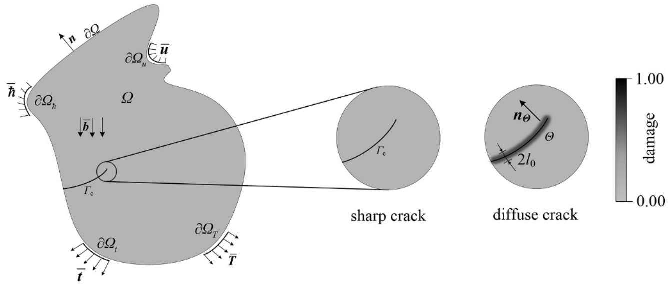

Fig. 2. Separation of solid crack faces and their diffuse characterization.

efficacy of the phase-field method.

Drawing on the unified phase-field theory developed by Wu et al. [28], and integrating the mixed-mode fracture phase-field model that includes the unified tensile fracture criterion outlined by Wang et al. [29], this paper introduces a thermomechanical damage coupling model designed for mixed-mode failure situations. This model effectively reduces the phase-field model's sensitivity to the length scale parameter l_0, enhancing its applicability and accuracy in simulating complex fracture behaviors. The proposed phase-field model is capable of simulating Mode I fracture, Mode II fracture, and mixed-mode fracture (Mode I/II). Given that almost all devices in the field of electronic packaging are influenced by temperature, leading to complex thermal stress effects on electronic devices during service, applying the phase-field model to simulate failure and damage in the interconnect structures of TGV and TSV within electronic packaging is of significant importance for enhancing the reliability of packaging structures. The annealing temperature of TGV/TSV-Cu during actual manufacturing processes ranges from room temperature to 400 °C. To simulate the manufacturing environment of TGV/TSV-Cu, we selected the same temperature range. Although previous research has demonstrated that the mechanical properties of TGV/TSV-Cu are sensitive to temperature changes [30], in actual production, failure in the TGV/TSV structure primarily occurs in the glass substrate, which possesses brittle material properties and is not sensitive to temperature variations. This initial study focused on evaluating the feasibility of analyzing the package interconnect structure using the phase field model. To simplify the model and enhance computational efficiency, we assumed that material properties remain constant despite temperature changes, allowing us to easily observe the impact of factors such as TGV/TSV shape and copper wall thickness.

This paper is organized as follows: Section 2 introduces the basic principles of the thermomechanically coupled phase-field model, including its governing equations and related historical fields. Section 3 presents the numerical solution scheme for the phase-field model, as well as the modeling method for the microstructure of Cu in TSVs. In Section 4, the given scheme is used to study the cracking and failure behavior of the TGV model under temperature cycling. Based on the provided algorithm, Section 5 conducts a numerical analysis of the interface damage during the annealing of the TSV structure. The paper is concluded with some discussions and closing remarks.

2. Phase field framework for fracture

2.1. Mathematical description for phase field

Consider an elastic continuum body $\Omega \subset \mathbb{R}^{n_{\text{dim}}}$ $(n_{\text{dim}} = 1, 2)$ containing a crack Γ_c (as shown in Fig. 2), where the elastic body is subjected to displacements $\overline{\mathbf{u}}$, temperature $\overline{\mathbf{T}}$, traction forces $\overline{\mathbf{t}}$, and heat flow $\overline{\hbar}$. These forces act on Dirichlet-type boundaries $(\partial\Omega_u, \partial\Omega_T)$ and Neumann-type boundaries $(\partial\Omega_t, \partial\Omega_\hbar)$ respectively, with $\partial\Omega_u \cap \partial\Omega_t = \phi$, $\partial\Omega_u \cup \partial\Omega_t = \partial\Omega$, $\partial\Omega_T \cap \partial\Omega_\hbar = \phi$, $\partial\Omega_T \cup \partial\Omega_\hbar = \partial\Omega$. Here, $\partial\Omega$ represents the external boundary of Ω, and $\mathbf{n}$ denotes its outward normal vector to the boundary $\partial\Omega$.

To avoid various issues encountered in simulating sharp cracks Γ_c, the phase field model diffuses the crack within a band of finite width, transforming the discontinuous field on either side of the crack Γ_c into a continuous field within the localized damage band $\Theta \subset \Omega$, where the phase field $\Theta(\mathbf{x})$ is defined such that d ranges from 0 to 1. Areas outside the localized damage band (Ω/Θ) are unaffected by the crack. In the phase-field model, a length scale parameter l_0 is introduced to characterize the width of the diffuse local band. When $(l_0 \to 0)$, a sharp crack is reproduced. Within the damage band Γ_c, the variable d characterizes the degree of damage at a certain location within the solid. When $d = 0$, it indicates that the material is undamaged, whereas $d = 1$ signifies that complete fracture has occurred at that location.

The energy functional for damage simulation can be expressed as the sum of the solid's strain energy and the crack surface energy, that is [31]:

$$\Pi(\mathbf{u}, \Gamma_c) = \int_\Omega \psi_0(\boldsymbol{\varepsilon}(\mathbf{u}))\, d\Omega + G_c \int_{\Gamma_c} \mathrm{d}\Gamma_c - \int_{\partial\Omega} \overline{\mathbf{t}} \cdot \mathbf{u} d\partial\Omega - \int_\Omega \overline{\mathbf{b}} \cdot \mathbf{u} d\Omega \tag{1}$$

where G_c represents fracture toughness of material; $\mathbf{u}$ is the displacement field, and ψ_0 is the elastic strain energy density, which can be calculated through the strain tensor $\boldsymbol{\varepsilon}(\mathbf{u})$:

$$\psi_0 = \frac{1}{2}\left(\lambda \varepsilon_{ii}\varepsilon_{jj} + 2\mu \varepsilon_{ij}\varepsilon_{ij}\right) \tag{2}$$

in which λ and μ are the Lamé constants, with μ being the shear modulus. The components of the strain tensor can be expressed as:

$$\varepsilon_{ij} = \frac{1}{2}(u_{i,j} + u_{j,i}) \tag{3}$$

$u_{i,j}$ and $u_{j,i}$ are the displacement gradients.

To track the evolution of cracks, a crack surface density function can be introduced to regularize the crack surface, which can be expressed as:

$$E_{\Gamma_c} = \int_{\Gamma_c} \mathrm{d}\Gamma_c = \int_\Theta \gamma(d, \nabla d) d\Theta \tag{4}$$

where $\gamma(d, \nabla d)$ is the crack surface density function used to diffuse the crack, and its specific form is as follows:

$$\gamma(d, \nabla d) = \frac{1}{c_0}\left[\frac{1}{l_0}\alpha(d) + l_0|\nabla d|^2\right] \tag{5}$$

where ∇d is the gradient of the damage variable d, and l_0 is the length scale parameter intrinsic to the material, which governs the width of the diffuse damage zone (shown in Fig. 2). c_0 is a normalization constant that ensures the correct energy contribution in the limit as l_0 approaches zero, ensuring that the model recovers the sharp crack limit. c_0 can be expressed as

$$c_0 = 4\int_0^1 \sqrt{\alpha(\beta)}\mathrm{d}\beta \tag{6}$$

where $\alpha(d)$ is a function related to the damage variable d, and can be expressed as

$$\alpha(d) = \vartheta d + (1 - \vartheta)d^2 \geq 0 \quad , \forall d \in [0, 1] \tag{7}$$

and

$$\alpha(0) = 0, \quad \alpha(1) = 1, \quad \alpha'(d) \geq 0 \tag{8}$$

where $\vartheta \in [0, 2]$ and $\alpha'(d)$ is the derivative of $\alpha(d)$ with respect to d.

Currently, there are two types of phase field models, energy decomposition and non-decomposition, and many papers have proved that the results are similar [32]. For simplicity, we use the second type. When using this model, it is possible to achieve highly accurate computational results without the need to separate the elastic energy into compressive and tensile components. In this work, we adopt the hybrid model to study the damage and failure of material. The expression for the elastic potential energy can be written as:

$$\int_{\Omega}\psi_0(\boldsymbol{\varepsilon}(\boldsymbol{u}),d)d\Omega=\int_{\Omega}\omega(d)\psi(\boldsymbol{\varepsilon}(\boldsymbol{u}),d)d\Omega \tag{9}$$

$\psi_0(\varepsilon(\boldsymbol{u}),d)$ is the degraded elastic potential energy density, which depends on both the strain tensor $\varepsilon(\boldsymbol{u})$ and the damage variable d. $\omega(d)$ is the degradation function and

$$\omega(d)=\frac{1}{1+\phi(d)},$$

$$\phi(d)=\frac{a_1 d\cdot P(d)}{(1-d)^p},$$

$$P(d)=1+a_2 d+a_3 d^2+\cdots$$

where $p\geq 2$ is the exponent; $P(d)>0$ is a continuous polynomial; a_i $(i=1,2,3,\cdots)$ are coefficients determined by material properties. It should be noted that the values of $\omega(d)$ smoothly decrease with the increase of the phase field d, and must satisfy the following properties:

$$\omega(0)=1,\quad \omega(1)=0,\quad \omega(1)'=0,\quad \omega(d)'\leq 0$$

In traditional phase field models, a significant issue of crack scale sensitivity may arise: as the crack scale decreases, the ultimate bearing capacity (peak load) of the structure increases. To avoid such problem, this work adopts the form $\alpha(d)=d(2-d)$ derived in the unified phase field model proposed in [28]. Using Eq. (6) the values of c_0 can be determined to be π.

Based on the method from the literature [28], for the energy degradation function, this paper adopts a quadratic form, that is, $a_i=0$ $(i>3)$. For a_i $(i=1,2,3)$, it is represented as follows:

$$a_1=\frac{4}{c_0 l_0}\frac{EG_c}{f_t^2} \tag{10}$$

$$a_2=\frac{1}{2}\left[\left(-\frac{16\pi}{c_0}\frac{G_c}{{f_t}^2}k_0\right)^{\frac{2}{3}}+1\right]-(p+1) \tag{11}$$

$$a_3=\begin{cases}0, & p>2\\ \dfrac{1}{a_2}\left[\dfrac{1}{2}\left(\dfrac{c_0 w_c f_t}{2\pi G_c}\right)^2-(1+a_2)\right], & p=2\end{cases} \tag{12}$$

In the formula, k_0 (<0) is the initial slope of the selected softening curve, w_c is the final crack opening when the stress at the crack tip disappears, and f_t is the material's tensile failure strength. It should be noted that if more accurate calculation results are desired, one can opt for higher-order polynomial forms of $P(d)$, but this will significantly increase the computational effort.

The initial slope of the selected softening curve and the final crack opening can be calculated using the following formula:

$$k_0=-\frac{c_0}{16\pi}\frac{f_t^2}{G_c}[2(a_2+p+1)-1]^{3/2} \tag{13}$$

$$w_c=\frac{2\pi G_c}{c_0 f_t}\sqrt{2P(1)}\lim_{d^*\rightarrow 1}(1-d^*)^{1-p/2} \tag{14}$$

where $P(1)=1+a_2+a_3+\cdots$ is the value of the polynomial $P(d)$ when $d=1$. Once the required material properties and the type of softening curve are determined, the parameters in $P(d)$ and the final form of the degradation function can be established. The simulations discussed in this paper all use a linear softening model for the degradation function, with the parameter values as follows:

$$k_0=-\frac{f_t^2}{2G_c}, w_c=\frac{2G_c}{f_t}, p=2 \quad\Rightarrow\quad a_2=-\frac{1}{2}, a_3=0 \tag{15}$$

The phase field model adopted in this work significantly reduces the sensitivity of the phase field model to the parameter l_0 by introducing the tensile failure strength into the degradation function. This is a serious issue in some traditional phase field model theories, where the mechanical response of the material tends to be highly sensitive to l_0 [33]. Using the tensile failure of a 1D long rod, it can be concluded that when a point undergoes fracture failure, the maximum critical tensile stress reached at that point is [34]:

$$\sigma_c=\sqrt{\frac{4EG_c}{c_0 a_1 l_0}}=f_t \tag{16}$$

From the above Eq. (16), it can be observed that the value of the critical stress is equal to the tensile failure strength and is independent of l_0.

3. The governing equation for the crack phase field-displacement field

By using Eqs. (4) and (9), and introducing the phase field variable d, the regularized form of Eq. (1) can be obtained as follows:

$$\Pi(\mathbf{u},d)=\int_{\Omega}\psi(\boldsymbol{\varepsilon}(\mathbf{u}))d\Omega+G_c\int_{\Theta}\gamma(d,\nabla d)d\Theta-\int_{\partial\Omega}\bar{\mathbf{t}}\cdot\mathbf{u}d\partial\Omega-\int_{\Omega}\bar{\mathbf{b}}\cdot\mathbf{u}d\Omega \tag{17}$$

Taking the variation of the total potential energy of the elastic body with respect to the displacement field $\mathbf{u}$ and the phase field d, one can obtain:

$$\begin{aligned}\delta\Pi(\mathbf{u},d)=&\int_{\Omega}\boldsymbol{\sigma}(\mathbf{u},d):\delta\boldsymbol{\varepsilon}\,d\Omega+\int_{\Omega}\frac{\partial\psi(\boldsymbol{\varepsilon},d)}{\partial d}\delta d\,d\Omega\\ &+\int_{\Theta}G_c\left[\frac{\partial\gamma(d,\nabla d)}{\partial d}\delta d+\frac{\partial\gamma(d,\nabla d)}{\partial\nabla d}\cdot\delta(\nabla d)\right]d\Theta\\ &-\int_{\partial\Omega}\bar{\mathbf{t}}\cdot\delta\mathbf{u}\,d\partial\Omega-\int_{\Omega}\bar{\mathbf{b}}\cdot\delta\mathbf{u}\,d\Omega\end{aligned} \tag{18}$$

where $\boldsymbol{\sigma}(\mathbf{u},d)=\frac{\partial\psi(\boldsymbol{\varepsilon},d)}{\partial\boldsymbol{\varepsilon}}$ is the stress tensor that depends on both the displacement field $\mathbf{u}$ and the phase field d, and $\delta\varepsilon$ is the variation of the strain tensor. Applying the principle of minimum energy and the divergence theorem to Eq. (18), the governing equations of the phase field model are derived as follows:

$$div\boldsymbol{\sigma}(\mathbf{u},d)+\bar{\mathbf{b}}=0\quad\text{in}\ \Omega \tag{19}$$

$$\left\{\begin{array}{ll}G_c\nabla\cdot\left(\dfrac{\partial\gamma(d,\nabla d)}{\partial\nabla d}\right)-G_c\dfrac{\partial\gamma(d,\nabla d)}{\partial d}-\dfrac{\partial\psi(\boldsymbol{\varepsilon},d)}{\partial d}=0, & \delta d>0\\ G_c\nabla\cdot\left(\dfrac{\partial\gamma(d,\nabla d)}{\partial\nabla d}\right)-G_c\dfrac{\partial\gamma(d,\nabla d)}{\partial d}-\dfrac{\partial\psi(\boldsymbol{\varepsilon},d)}{\partial d}<0, & \delta d=0\end{array}\right.\quad\text{in}\ \Theta \tag{20}$$

By substituting Eq. (4) into Eq. (20), the following set of equations is derived, valid within the domain Θ:

$$\begin{cases}\dfrac{2G_c l_0}{c_0}\nabla^2 d-\dfrac{G_c}{c_0 l_0}\alpha'(d)-\omega'(d)\psi_0=0, & \delta d>0\\ \dfrac{2G_c l_0}{c_0}\nabla^2 d-\dfrac{G_c}{c_0 l_0}\alpha'(d)-\omega'(d)\psi_0<0, & \delta d=0\end{cases} \tag{21}$$

The boundary conditions for the system are specified as follows:

$$\begin{cases}\boldsymbol{\sigma}(\mathbf{u},d)\cdot\mathbf{n}=\bar{\mathbf{t}} & \text{on}\quad\partial\Omega_t\\ \nabla d\cdot\mathbf{n}_\Theta\geq 0 & \text{on}\quad\partial\Theta\end{cases} \tag{22}$$

where ∇d is the gradient of the phase field, and $\mathbf{n}_\Theta$ is the outward normal vector to the boundary $\partial\Theta$. Eq. (19) is referred to as the elasticity equation, used to solve for the displacement field, while Eq. (21) is known as the crack evolution equation, utilized to calculate the distribution of the phase field.

3.1. Phase-field model for mixed-mode tension-shear failure

The phase-field model for tension-shear failure involves using phase-field theory to simulate material behavior under simultaneous tension and shear stresses. This model is crucial in materials science and structural engineering, as it helps researchers understand and predict how materials fail under complex stress conditions. Based on the mixed-mode phase field theory for tension-shear mixed failure modes proposed in [29], the energy density function is decomposed using two different degradation functions as:

$$\psi_0 = \omega_I(d)\psi_{0I}^{+} + \omega_{II}(d)\psi_{0II}^{+} + \psi_0^{-} \tag{23}$$

in which ψ_{0I}^{+} is the tensile strain energy density caused by the normal tensile stress at a point on the plane, ψ_{0II}^{+} is the shear strain energy density caused by the shear stress on the same plane, and ψ_0^{-} represents the remaining strain energy. ω_I and ω_{II} correspond to the degradation functions for the tensile strain energy ψ_{0I}^{+} and the shear strain energy ψ_{0II}^{+}, respectively. For the plane stress state, the components of the strain energy density can be calculated as follows:

$$\psi_{0I}^{+} = \begin{cases} \dfrac{(\overline{\boldsymbol{\sigma}}^{rr})^2}{2E} & \text{if} \quad \overline{\boldsymbol{\sigma}}^{rr} > 0 \\ 0 & \text{if} \quad \overline{\boldsymbol{\sigma}}^{rr} \leq 0 \end{cases} \tag{24}$$

$$\psi_{0II}^{+} = \begin{cases} \dfrac{(\overline{\boldsymbol{\sigma}}^{rm})^2}{2\mu} = \dfrac{\overline{\tau}^2}{2\mu} & \text{if} \quad \overline{\boldsymbol{\sigma}}_1 > 0 \\ 0 & \text{if} \quad \overline{\boldsymbol{\sigma}}_1 \leq 0 \end{cases} \tag{25}$$

$$\psi_0^{-} = \psi_0 - \psi_{0I}^{+} - \psi_{0II}^{+} \tag{26}$$

where *r* and *m* respectively represent the unit normal vector and the unit tangential vector on the plane. $\overline{\boldsymbol{\sigma}}^{rr}$ and $\overline{\boldsymbol{\sigma}}^{rm}$ are the effective normal stress and effective shear stress on the plane, respectively. $\overline{\boldsymbol{\sigma}}_1$ is the first principal stress of the effective stress tensor $\overline{\boldsymbol{\sigma}}$, and the relationship between $\overline{\boldsymbol{\sigma}}$ and $\boldsymbol{\sigma}$ can be obtained from the following equation:

$$\begin{bmatrix} \overline{\boldsymbol{\sigma}}^{rr} \\ \overline{\boldsymbol{\sigma}}^{rm} \\ \overline{\boldsymbol{\sigma}}^{rm} \end{bmatrix} = \begin{bmatrix} \dfrac{1}{\omega_I(d)} & 0 & 0 \\ 0 & \dfrac{1}{\omega_I(d)} & 0 \\ 0 & 0 & \dfrac{1}{\omega_{II}(d)} \end{bmatrix} \begin{bmatrix} \boldsymbol{\sigma}^{rr} \\ \boldsymbol{\sigma}^{rm} \\ \boldsymbol{\sigma}^{rm} \end{bmatrix} \tag{27}$$

in which

$$\omega_I = \frac{1}{1+\varphi_I(d)} \tag{28}$$

$$\omega_{II} = \frac{1}{1+\varphi_{II}(d)} \tag{29}$$

The crack evolution equation for the tensile-shear failure mode is

$$\omega_I'(d)\frac{\psi_{0I}^{+}}{G_{cI}} + \omega_{II}'(d)\frac{\psi_{0II}^{+}}{G_{cII}} \geq \frac{2l_0^2\nabla^2 d - \alpha'(d)}{c_0 l_0} \tag{30}$$

G_{cI} and G_{cII} are respectively the fracture toughnesses for pure tensile failure and pure shear failure, and can be expressed as:

$$G_{cI} = \frac{c_0 l_0}{2E}\frac{\phi'(0)}{\alpha'(0)}\boldsymbol{\sigma}_t^2 \tag{31}$$

$$G_{cII} = \frac{\chi^2 E}{\mu} G_{cI} \tag{32}$$

where $\boldsymbol{\sigma}_t$ is the critical tensile failure strength; χ is the ratio of the critical shear strength $\boldsymbol{\tau}_s$ to the critical tensile strength $\boldsymbol{\sigma}_t$. For more details, please refer to reference [29].

3.2. Irreversibility of damage

To prevent the phenomenon of crack healing in computation, it is necessary to use a strain energy history function

$$\mathscr{H} = max\left(\overline{Y}_0, \max_{n\in[0,T]} \overline{Y}_n\right) \tag{33}$$

to replace $\psi_0(\boldsymbol{\varepsilon}(\mathbf{u}), d)$ in the crack evolution Eq. (21) to express the irreversibility of damage, i.e., $\dot{d} \geq 0$. The strain energy history function $\mathscr{H}$ is a historical state variable, also known as a history field variable. It characterizes the maximum tensile strain energy reached at a given location throughout the loading history. This ensures that the damage evolution model accounts for the cumulative effect of loading, reflecting the material's irreversible nature of damage under mechanical stresses. By tracking the highest level of strain energy experienced, $\mathscr{H}$ effectively prevents the artificial healing of cracks and ensures that the damage progression in the material is consistent with physical observations and the thermodynamic principles governing fracture mechanics. $\overline{Y}_0$ is the initial strain energy density or a reference strain energy density value. $\overline{Y}_n$ represents the strain energy density at any previous time *n* within the interval $[0, T]$. Y_0 and Y_n can respectively be expressed as:

$$\overline{Y}_0 = \frac{1}{2EG_c} f_t^2 = \frac{\alpha'(0)}{c_0 l_0 \phi'(0)} \tag{34}$$

$$\overline{Y}_n = \frac{1}{2EG_c}\langle\overline{\sigma}_1\rangle^2 \tag{35}$$

Therefore, the governing equations of the phase field model can be further rewritten as:

$$\begin{cases} div\boldsymbol{\sigma}(\mathbf{u}, d) + \overline{\mathbf{b}} = 0 & \text{in } \Omega \\ \omega'(d)\mathscr{H} = \dfrac{2l_0^2\nabla^2 d - \alpha'(d)}{c_0 l_0} & \text{in } \Theta \end{cases} \tag{36}$$

In practical implementation, the phase field model can indeed be viewed as a multi-field coupling problem of the displacement field and the phase field. Consequently, the elasticity equation and the crack evolution Eq. (36), along with their boundary conditions (22), can be rewritten in a similar form:

$$\begin{cases} \nabla\cdot\boldsymbol{\sigma} + \overline{\mathbf{b}} = 0 & \text{in } \Omega \\ \boldsymbol{\sigma}\cdot\mathbf{n} = \overline{\mathbf{t}} & \text{on } \partial\Omega \end{cases} \tag{37}$$

$$\begin{cases} \nabla\cdot\boldsymbol{q} + Q(d) = 0 & \text{in } \Theta \\ \boldsymbol{q}\cdot\mathbf{n}_\Theta \geq 0 & \text{on } \partial\Theta \end{cases} \tag{38}$$

Eq. (37) provided is indeed the elasticity equations for solving the displacement field problem, which ensure mechanical equilibrium within the material domain Ω. Eq. (38) represents the crack evolution equations for solving the phase field problem within the domain Θ. The flux vector $\boldsymbol{q}$ could be related to the gradient of the phase field variable *d*, and $Q(d)$ represents the source term that is dependent on the damage or phase field variable *d*. $\boldsymbol{q}$ and $Q(d)$ can be obtained by following

$$\begin{cases} \boldsymbol{q} = \dfrac{2l_0}{c_0}\nabla d \\ Q(d) = -\omega'(d)\mathscr{H} - \dfrac{1}{c_0 l_0}\alpha'(d) \end{cases} \tag{39}$$

3.3. The thermal-mechanical-damage coupling model

To describe the process of heat conduction in solids, the following

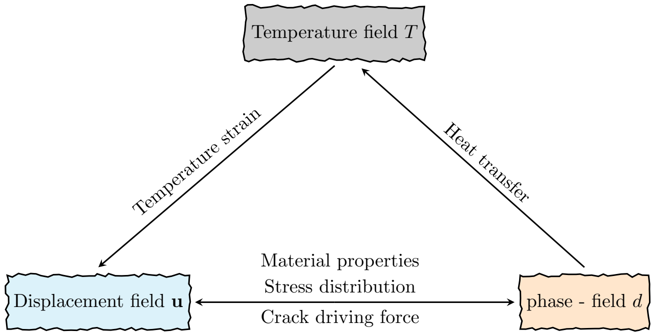

Fig. 3. The interaction relationships among the field variables in a coupled thermo-mechanical-damage model.

partial differential equation is introduced:

$$\begin{cases} \rho c_T \dot{T} + \nabla \cdot \boldsymbol{\hbar} = \overline{\gamma} & \text{in } \Omega \\ \boldsymbol{\hbar} \cdot \mathbf{n} = \overline{\boldsymbol{\hbar}} & \text{on } \partial\Omega_{\hbar} \end{cases} \tag{40}$$

where ρ is the density of the material; c_T is the specific heat capacity at constant pressure. $\dot{T}$ represents the time derivative of the temperature field T, indicating how the temperature changes over time within the solid. $\nabla \cdot \boldsymbol{\hbar}$ denotes the divergence of the heat flux vector $\boldsymbol{\hbar}$, representing the rate at which heat is flowing out of or into a given volume. $\overline{\gamma}$ corresponds to any internal heat sources or sinks within the domain Ω. The second equation specifies the boundary condition on $\partial\Omega_{\hbar}$, the part of the boundary where heat flux is prescribed. Here, $\boldsymbol{\hbar} \cdot \mathbf{n}$ represents the heat flux across the boundary, with $\mathbf{n}$ being the outward normal vector, and $\overline{\boldsymbol{\hbar}}$ is the prescribed heat flux on the boundary. The heat flux $\boldsymbol{\hbar}$ can be obtained through the following Fourier's law:

$$\boldsymbol{\hbar} = -k_T \nabla T, \quad k_T = g(d) k_0 \tag{41}$$

where ∇T is the temperature gradient, the rate at which temperature changes with distance within the material. k_T represents the degraded thermal conductivity, which ensures that there is no heat flow across the crack as it opens. It is determined by a degradation function $g(d)$ controlled by the phase field variable d. k_0 is the thermal conductivity of the material, a measure of its ability to conduct heat. This work adopts a commonly used form of the degradation function, which is $g(d) = \omega(d)$.

According to the principles of kinematics, the strain under the assumption of small deformations can be expressed as:

$$\boldsymbol{\varepsilon} = \frac{1}{2}\left(\nabla \mathbf{u} + (\nabla \mathbf{u})^T\right) \tag{42}$$

where $\boldsymbol{\varepsilon}$ is the strain tensor, $\nabla \mathbf{u}$ is the gradient of the displacement vector $\mathbf{u}$, $(\nabla \mathbf{u})^T$ is the transpose of the gradient of the displacement vector.

For thermo-mechanical coupling problems, the total strain $\boldsymbol{\varepsilon}$ can be decomposed into elastic strain ($\boldsymbol{\varepsilon}_e$) and thermal strain ($\boldsymbol{\varepsilon}_T$) components. This can be expressed as:

$$\boldsymbol{\varepsilon} = \boldsymbol{\varepsilon}_e + \boldsymbol{\varepsilon}_T \tag{43}$$

The thermal strain component is often modeled as proportional to the temperature change ($\Delta T = T - T_0$) from a reference temperature or initial temperature T_0, typically using the linear thermal expansion coefficient (α_0) of the material:

$$\boldsymbol{\varepsilon}_T = \alpha_0 \Delta T I$$

where I is the identity tensor, ensuring that the thermal strain is isotropic (uniform in all directions).

Therefore, the thermo-mechanical-damage coupled equations can be derived by combining Eqs. (37), (38) and (40). The coupled partial differential equations for a thermo-mechanical-damage model can be written as:

$$\begin{cases} \nabla \cdot \boldsymbol{\sigma} + \overline{\mathbf{b}} = 0 & \text{in } \Omega \\ \rho c_T \dot{T} + \nabla \cdot \boldsymbol{\hbar} = \overline{\gamma} & \text{in } \Omega \\ \nabla \cdot \mathbf{q} + Q(d) = 0 & \text{in } \Theta \end{cases} \tag{44}$$

and its boundary conditions are:

$$\begin{cases} \boldsymbol{\sigma} \cdot \mathbf{n} = \overline{\mathbf{t}} & \text{on } \partial\Omega_t \\ \boldsymbol{\hbar} \cdot \mathbf{n} = \overline{\hbar} & \text{on } \partial\Omega_{\hbar} \\ \mathbf{q} \cdot \mathbf{n}_{\Theta} \geq 0 & \text{on } \partial\Theta \end{cases} \tag{45}$$

In the computation, there are three fundamental field variables to be determined: the displacement field $\boldsymbol{u}$, the phase field d, and the temperature field T. The diagram in Fig. 3 showcases the interactions among these field variables, where thermal strain induced by temperature changes leads to alterations in deformation. Subsequently, the growth in deformation increases the effective crack driving force, further promoting crack evolution. In turn, these cracks cause the degradation of material properties, thereby affecting the stress distribution and the heat conduction process within the simulated object. In the multi-field coupled phase field model proposed in this work, 9 material properties need to be obtained in advance as input parameters for the calculation. These variables are: elastic modulus E, Poisson's ratio ν, tensile failure strength f_t, fracture toughness G_c, mass density ρ, thermal conductivity k_0, specific heat capacity c_T, thermal expansion coefficient α_0, critical shear-to-normal stress ratio χ.

4. Implementation of the phase field scheme

To develop a finite element model, it is essential to convert the strong forms of the governing equations into their corresponding weak forms. The weak form is obtained by multiplying each equation in Eq. (44) by an appropriate arbitrary test function and then integrating over the domain. Following partial integration, the weak forms are then articulated as follows:

$$\begin{aligned} &\int_{\Omega} \boldsymbol{\sigma} : \nabla \delta_u dV + \int_{\Omega} \overline{\mathrm{b}} \cdot \delta_u \mathrm{d}V - \int_{\Omega_t} \overline{\boldsymbol{t}} \cdot \delta_u \mathrm{d}A = 0, \\ &\int_{\Omega} \rho c_T \dot{T} \delta_T \,\mathrm{d}V + \int_{\Omega} \boldsymbol{\hbar} \cdot \nabla(\delta_T)\,\mathrm{d}V - \int_{\Omega} \overline{\gamma} \delta_T dV - \int_{\Omega_h} \overline{\boldsymbol{\hbar}} \cdot \delta_T dA = 0, \\ &\int_{\Theta} (\boldsymbol{q} \cdot \nabla \delta_d - Q \delta_d)\,\mathrm{d}V = 0. \end{aligned} \tag{46}$$

For a 2D FEM where each node has four degrees of freedom (DOFs), comprising two for the displacement field (u_x and u_y), one for the temperature field (T), and one for the phase field (d), the approximation of these field variables and their derivatives at any point $\boldsymbol{x}$ within an element e with I nodes can be expressed using shape functions and nodal values. Here's a general form for these approximations:

- Displacement field $\mathbf{u}(u_x, u_y)$:

$$\begin{aligned} u_x(\mathbf{x}) &= \sum_{i=1}^{I} N_i(\mathbf{x}) u_{x,i} \\ u_y(\mathbf{x}) &= \sum_{i=1}^{I} N_i(\mathbf{x}) u_{y,i} \end{aligned} \tag{47}$$

where $u_{x,i}$ and $u_{y,i}$ are the displacement components at node i, and $N_i(x)$ is the shape function associated with node i.

- Temperature field T:

$$T(\mathbf{x}) = \sum_{i=1}^{I} N_i(\mathbf{x}) T_i \tag{48}$$

where T_i is the temperature at node i.

- Phase field d:

$$d(\mathbf{x}) = \sum_{i=1}^{I} N_i(\mathbf{x}) d_i \tag{49}$$

where d_i is the damage variable at node i.

The gradients or partial derivatives of these fields can be approximated similarly by taking the derivatives of the shape functions with respect to spatial coordinates.

- Displacement gradient:

$$\begin{aligned} \nabla u_x(\mathbf{x}) &= \sum_{i=1}^{I} \nabla N_i(\mathbf{x}) u_{x,i} \\ \nabla u_y(\mathbf{x}) &= \sum_{i=1}^{I} \nabla N_i(\mathbf{x}) u_{y,i} \end{aligned} \tag{50}$$

- Temperature gradient:

$$\nabla T(\mathbf{x}) = \sum_{i=1}^{I} \nabla N_i(\mathbf{x}) T_i \tag{51}$$

- Damage gradient:

$$\nabla d(\mathbf{x}) = \sum_{i=1}^{I} \nabla N_i(\mathbf{x}) d_i \tag{52}$$

These approximations are fundamental in the finite element analysis, allowing the transformation of the continuous problem into a discrete one that can be solved computationally. The shape functions $N_i(\mathbf{x})$ are chosen based on the element type (e.g., linear, quadratic) and determine the accuracy and convergence of the solution. The gradients of the shape functions $\nabla N_i(\mathbf{x})$ are used to compute the strain and heat flux within the element, which are critical for evaluating the element's stiffness matrix, force vector, and other properties related to the problem's physics.

Based on the finite element discretization described earlier, and aiming to drive the residuals towards zero, the residual vectors for displacement ($\mathbf{g}_u$), temperature ($\mathbf{g}_T$), and damage ($\mathbf{g}_d$) within the context of a coupled thermo-mechanical-damage finite element model can be formulated as follows:

- Displacement residual vector ($\mathbf{g}_u$):

$$\mathbf{g}_{\mathbf{u}} := \mathbf{f}_{\mathbf{u}}^{\text{ext}} - \int_{\Omega} \mathbf{B}_{\mathbf{u}}^{\mathrm{T}} \boldsymbol{\sigma} \mathrm{dV} = \mathbf{0} \tag{53}$$

$\boldsymbol{\sigma}$ is the stress tensor calculated from the current state of strain in the material, and $\mathbf{B}_u$ is the displacement-strain matrix that relates nodal displacements to strains. $\mathbf{f}_u^{\text{ext}}$ is the external force vector acting on the system and can be expressed as

$$\mathbf{f}_u^{\text{ext}} = \int_{\Omega} \mathbf{N}_u^{\mathrm{T}} \overline{\mathbf{b}} \mathrm{d}V + \int_{\partial\Omega} \mathbf{N}_u^{\mathrm{T}} \overline{\mathbf{t}} \mathrm{d}A \tag{54}$$

where $\mathbf{N}_u^{\mathrm{T}}$ is the transpose of the shape function matrix for the displacement field, mapping the effects of forces to nodal displacements. $\overline{\mathbf{b}}$ represents the body force vector per unit volume, acting throughout the material's volume Ω. $\overline{\mathbf{t}}$ denotes the surface traction vector applied on the boundary $\partial\Omega$.

- Temperature residual vector ($\mathbf{g}_T$):

$$\mathbf{g}_T := \mathbf{f}_T^{\text{ext}} + \int_{\Omega} \mathbf{B}_T^{\mathrm{T}} \boldsymbol{\hbar} \mathrm{d}V - \mathbf{C} \dot{\widetilde{T}} = \mathbf{0} \tag{55}$$

$\mathbf{B}_T$ is the temperature gradient matrix, and $\dot{\widetilde{T}} = d\widetilde{T}/dt$ is the rate of change of temperature at the nodes. $\mathbf{C}$ is the heat capacity matrix, and

$$\mathbf{C} = \int_{\Omega} \rho c_T \mathbf{N}_T^{\mathrm{T}} \mathbf{N}_T \mathrm{d}V \tag{56}$$

Here, $\mathbf{N}_T$ is the shape function matrix for the temperature field, used for interpolating temperature values within each finite element from nodal temperatures. $\mathbf{N}_T^{\mathrm{T}}$ denotes the transpose of the temperature shape function matrix. In Eq. (55), $\mathbf{f}_T^{\text{ext}}$ is the external heat flux vector and can be obtained by two main parts: the internal heat generation within the domain Ω and the heat flux across its boundary $\partial\Omega_{\hbar}$. Here's a breakdown of the equation:

$$\mathbf{f}_T^{\text{ext}} = \int_{\Omega} \mathbf{N}_T^{\mathrm{T}} \overline{\gamma} \mathrm{d}V - \int_{\partial\Omega_{\hbar}} \mathbf{N}_T^{\mathrm{T}} \overline{\boldsymbol{\hbar}} \mathrm{d}A \tag{57}$$

- Damage residual vector ($\mathbf{g}_d$):

$$\mathbf{g}_d := \int_{\Omega} \mathbf{N}_d^{\mathrm{T}} Q \mathrm{d}V - \int_{\Theta} \mathbf{B}_d^{\mathrm{T}} \boldsymbol{q} \mathrm{d}V = \mathbf{0} \tag{58}$$

$\mathbf{N}_d$ is the shape function matrix for the damage variable, Q represents the source term for damage evolution, and $\boldsymbol{q}$ is the damage flux, indicating how damage spreads within the material. $\mathbf{B}_d$ relates the gradients of the damage variable to nodal values.

Driving these residuals in Eqs. (53), (55) and (58) to zero ensures that the simulated responses (mechanical deformation, temperature distribution, and damage evolution) accurately reflect the physical behavior under given loading and boundary conditions.

When the computation process is discretized into N sub-time step $[t_n, t_{n+1}]$ $(n = 0, 1, 2, \cdots, N-1)$, the rate of change of nodal temperature $\dot{\widetilde{T}}$ within sub-time step i can be defined as:

$$\dot{\widetilde{T}} = \frac{\widetilde{T}_{n+1} - \widetilde{T}_n}{\Delta t} \quad \text{with} \quad \Delta t = t_{n+1} - t_n \tag{59}$$

where $\widetilde{T}_{n+1}$ is the nodal temperature vector at the end of the current time step $n+1$. $\widetilde{T}_n$ is the nodal temperature vector at the end of the previous time step n. Δt is the duration of the time step.

Therefore, the residual vector for the temperature field in Eq. (55) can be approximated in the following form:

$$\mathbf{g}_T := \Delta t \mathbf{f}_T^{\text{ext}} + \Delta t \int_{\Omega} \mathbf{B}_T^{\mathrm{T}} \boldsymbol{\hbar} \mathrm{d}V - \mathbf{C}(\widetilde{T}_{n+1} - \widetilde{T}_n) = \mathbf{0} \tag{60}$$

The equation essentially balances the external thermal loads and the change in internal thermal energy against the heat conduction within the material for a discrete time step. The goal is to find $\widetilde{T}_{n+1}$, the nodal temperature vector for the current time step, such that the thermal equilibrium condition represented by $\mathbf{g}_T = \mathbf{0}$ is satisfied. This involves solving for $\widetilde{T}_{n+1}$ that minimizes the residual, thus ensuring that the simulated temperature distribution aligns with the physical behavior dictated by the heat conduction and storage within the material under the applied thermal loads.

Due to the nonlinear nature of the equations in the coupled thermo-mechanical-damage problem, to enhance the numerical solution's convergence, a staggered iterative solution algorithm is adopted in solving the control equations. This approach involves alternately solving subsets of the coupled equations with the aim of achieving convergence in a stepwise manner. Dividing the control equations into thermo-mechanical coupling subproblems and damage subproblems, and then alternately fixing the thermo-mechanical coupling subproblems and the damage subproblems, represents a staggered approach to solving the coupled system.

Initially, by fixing the phase field variables, one can solve for the displacement and temperature variables $(\boldsymbol{u}, T)$. Subsequently, the obtained displacement and temperature fields are further utilized to calculate the phase field d. This sequential approach delineates a clear path for solving coupled problems in a staggered manner, enhancing both computational efficiency and convergence stability in simulations involving complex interactions between mechanical deformation, thermal effects, and material degradation. Here's a step-by-step breakdown of this process for the jth step of interval $[t_n, t_{n+1}]$:

Step 1: Evaluation of displacement and temperature fields.

Start the iteration by treating the phase field d as known or fixed, either from initial conditions or from the previous iteration's results. Then, we can solve the following equations of the thermo-mechanical coupling problem to obtain the displacement and temperature fields.

$$\begin{cases} \mathbf{g}_u\left(\tilde{\boldsymbol{u}}^{(j)}_{n+1}\right) := \mathbf{f}^{\text{ext}}_{u,n+1} - \int_\Omega \mathbf{B}_u^T \boldsymbol{\sigma}\, \mathrm{d}V = \mathbf{0}, \quad \boldsymbol{\sigma} = \boldsymbol{\sigma}\left(\tilde{\boldsymbol{u}}^{(j)}_{n+1}, \tilde{T}^{(j)}_{n+1}, \tilde{d}^{(j-1)}_{n+1}\right) \\ \mathbf{g}_T\left(\tilde{T}^{(j)}_{n+1}\right) := \Delta t \mathbf{f}^{\text{ext}}_{T,n+1} + \Delta t \int_\Omega \mathbf{B}_T^{\mathrm{T}} \boldsymbol{\hbar}\, \mathrm{d}V - \mathbf{C}\left(\tilde{T}_{n+1} - \tilde{T}_n\right) = \mathbf{0}, \quad \boldsymbol{\hbar} = \boldsymbol{\hbar}\left(\tilde{T}^{(j)}_{n+1}, \tilde{d}^{(j-1)}_{n+1}\right) \end{cases} \tag{61}$$

The sub-problem is solved using the Newton-Raphson method, and its linear equation can be formulated as follows

$$\begin{bmatrix} \mathbf{K}_{uu} & \mathbf{K}_{uT} \\ \mathbf{0} & \mathbf{K}_{TT} \end{bmatrix} \begin{Bmatrix} \delta\tilde{\mathbf{u}} \\ \delta\tilde{T} \end{Bmatrix} = \begin{Bmatrix} \mathbf{g}_u \\ \mathbf{g}_T \end{Bmatrix} \tag{62}$$

and

$$\mathbf{K}_{uu} = \int_\Omega \mathbf{B}_u^{\mathrm{T}} \left(\frac{\partial \boldsymbol{\sigma}}{\partial \boldsymbol{\varepsilon}}\right) \mathbf{B}_u \mathrm{d}V \tag{63}$$

$$\mathbf{K}_{uT} = \int_\Omega \mathbf{B}_u^{\mathrm{T}} \left(\frac{\partial \boldsymbol{\sigma}}{\partial T}\right) \mathbf{N}_T \mathrm{d}V \tag{64}$$

$$\mathbf{K}_{TT} = \Delta t \int_\Omega \mathbf{B}_T^{\mathrm{T}} k_T \mathbf{B}_T \ \mathrm{d}V + C \tag{65}$$

It's important to note that the proposed model takes into consideration the strain induced by temperature changes and assumes that strain/stress does not affect the heat conduction process. This is the reason why $K_{Tu} = 0$ while $K_{uT} \neq 0$ in the Eq. (62).

Step 2: Update phase field.

With $\tilde{\boldsymbol{u}}^{(j)}_{n+1}$ and $\tilde{T}^{(j)}_{n+1}$ now known, proceed to update the phase field. And solve the damage evolution equation to compute $\tilde{d}^{(j)}_{n+1}$, considering the influences of mechanical stresses (derived from $\boldsymbol{u}^{(j)}_{n+1}$) and temperature ($\tilde{T}^{(j)}_{n+1}$) by the following equation:

$$\mathbf{g}_d\left(\tilde{d}^{(j)}_{n+1}\right) := \int_\Omega \mathbf{N}_d^{\mathrm{T}} Q \mathrm{d}V - \int_\Theta \mathbf{B}_d^{\mathrm{T}} q \mathrm{d}V = \mathbf{0}, \quad Q = Q\left(\tilde{u}^{(j)}_{n+1}, \tilde{T}^{(j)}_{n+1}, \tilde{d}^{(j)}_{n+1}\right), \quad \mathbf{q} = \mathbf{q}\left(\tilde{d}^{(j)}_{n+1}\right) \tag{66}$$

The above process is repeated in a loop within each load step until the final solutions for all fields ($\boldsymbol{u}$, T, d) converge to within a specified tolerance. More details on the staggered iterative solution strategy are presented in Algorithm 1 [35].

Algorithm 1 Staggered Minimization for Coupled Thermo-Mechanical-Damage Model

```
Input: Initial conditions for $T$, $\mathbf{u}$, and $d$; material properties; external forces and thermal loads; tolerance $\epsilon$.
Output: Converged solutions for $T$, $\mathbf{u}$, and $d$ fields.
Initialization: Set initial conditions for $T_0$, $\mathbf{u}_0$, and $d_0$. Initialize iteration counter: $j = 0$.
while convergence not achieved do
    $j = j + 1$
    Step 1: Solve Thermo-Mechanical Subproblem
    Fix $d_{j-1}$.
    Solve for $T_j$ and $u_j$ considering the fixed $d_{j-1}$:
        Thermal Analysis: Solve the heat conduction equation to update $T_j$.
        Mechanical Analysis: Solve the mechanical equilibrium equations to update $u_j$.
    Step 2: Solve Damage Subproblem
    With $T_j$ and $u_j$ fixed, solve for $d_j$:
        Damage Analysis: Update $d_j$ using the damage evolution model based on current states of $T_j$ and $u_j$.
    Step 3: Check Convergence
    Calculate residuals for $T$, $\mathbf{u}$, and $d$.
    if $||\mathbf{g}_T|| < \epsilon$ and $||\mathbf{g}_u|| < \epsilon$ and $||\mathbf{g}_d|| < \epsilon$ then
        Convergence achieved; break.
    end if
end while
Post-Processing: Analyze and visualize the converged fields $T$, $\mathbf{u}$, and $d$.
End Algorithm.
```

There are two types of phase field models based on the solution strategy: implicit and explicit. Since the cases addressed in this work is a kind of static problem, the commonly used implicit solver is employed. In [36], the authors provide an overview of both implicit and explicit phase field models for quasi-static failure processes, including detailed discussions on their theories and implementation in the commercial

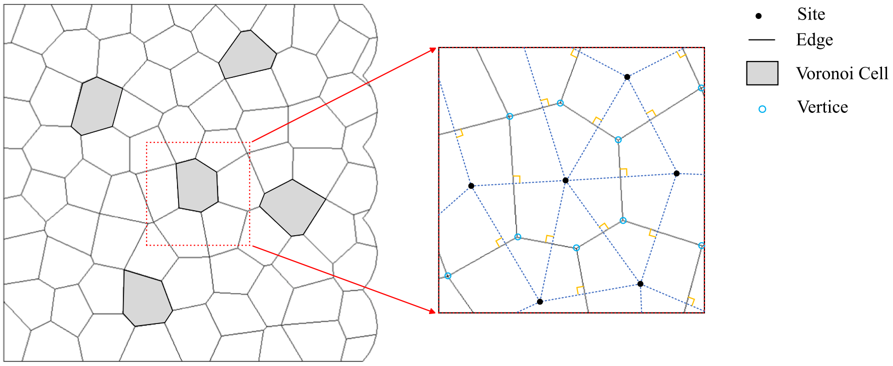

Fig. 4. Construction of Voronoi cells.

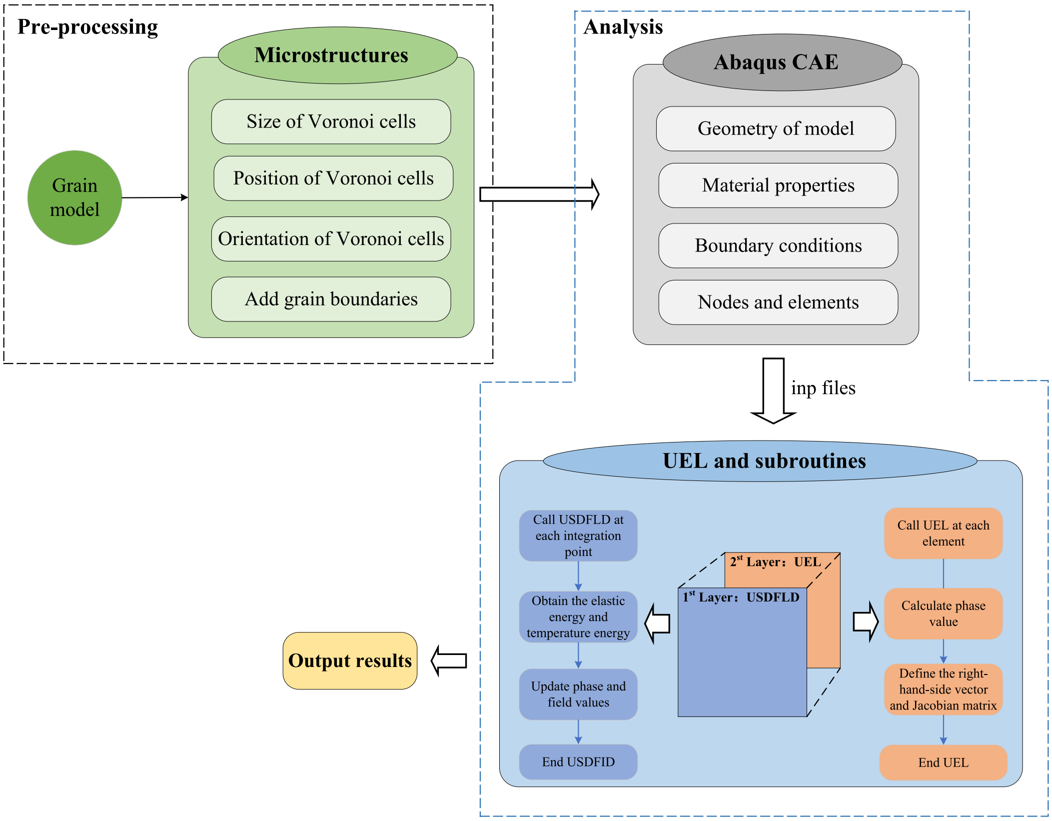

Fig. 5. The scheme of proposed simulation.

software ABAQUS. Interested readers can refer to this work for further information.

5. Numerical scheme for phase field simulation of thermoelastic microstructure

In this section, the approach for phase field simulation of thermoelastic microstructure of the seed layer was proposed, as shown in Fig. 5. The approach to studying coupled thermo-mechanical-damage models can indeed be divided into two parts, focusing first on microstructure generation using Voronoi polygons and second on conducting phase field simulations to analyze mechanical and fracture behaviors. This division allows for a detailed examination of material properties from a microstructural perspective, followed by an exploration of how these microstructures influence macroscopic properties under various loading conditions.

Voronoi polygons are a way of dividing space into regions based on distances to a specified set of points. These regions, or Voronoi cells, are defined such that every point in a given cell is closer to its corresponding site point than to any other site point. Generating Voronoi polygons can be approached through several computational steps, typically involving algorithms designed to efficiently partition space. Here's a simplified overview of the process and a model of Voronoi polygons is shown in Fig. 4:

- Set Up the Points (Sites): The process begins with a set of points in a plane, which will serve as the sites for the Voronoi diagram.
- Determine the Edges: For each pair of points, find the perpendicular bisector of the line segment connecting them. The perpendicular bisectors will serve as potential edges of the Voronoi cells.

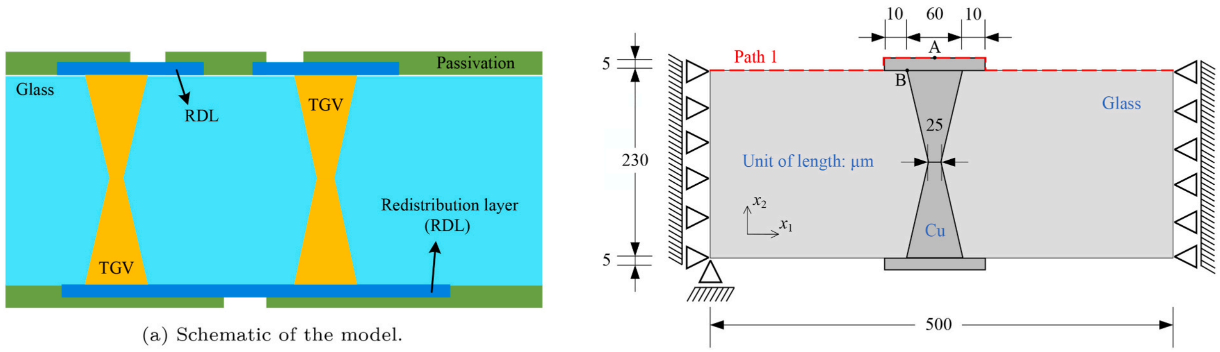

(a) Schematic of the model.

(b) Geometric parameters and boundary conditions.

Fig. 6. The considered TGV model.

Table 1
Material parameters used in the computation [37,38].

Material	Glass	Cu
Young's modulus E (GPa)	77.80	128.00
Poisson's ratio ν	0.17	0.30
Density ρ (kg/m^3)	2200.00	8960.00
Thermal conductivity coefficient (W m^{-1} K^{-1})	1.53	393.50
Specific heat capacity (J kg^{-1} K^{-1})	600.00	386.00
Thermal expansion coefficient α_0 (ppm/°C)	0.48	17.00
Tensile strength (MPa)	50.00	209.00
Fracture toughness (N/m)	8.00	690.30
Critical shear ratio χ	0.60	1.00

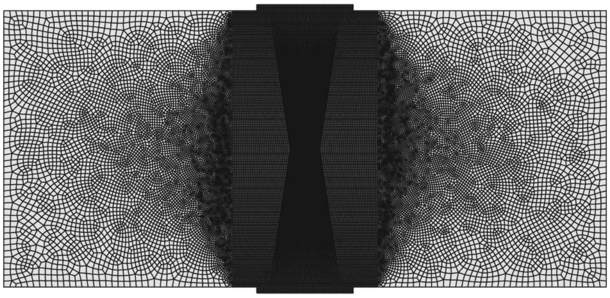

Fig. 7. Mesh of the TGV model.

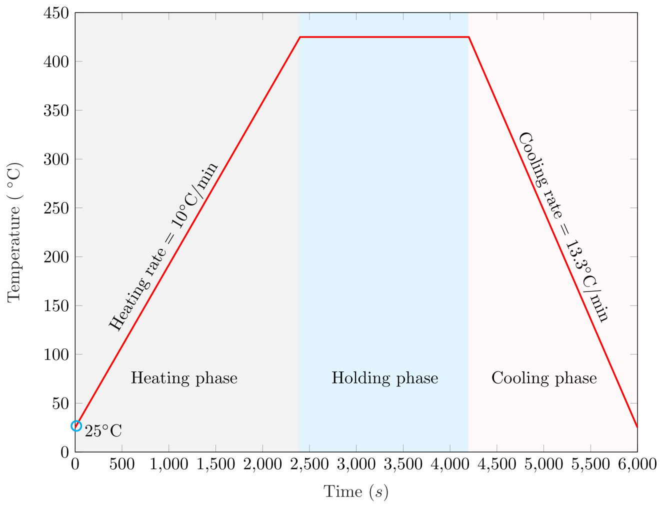

Fig. 8. Temperature loading curve.

- Identify the Vertices: The intersection points of the edges determined in the previous step serve as vertices of the Voronoi polygons. Each vertex is equidistant from at least three site points.
- Construct the Voronoi Cells: For each site point, construct a polygon (Voronoi cell) by connecting the vertices that are closest to that point and lie on the perpendicular bisectors determined earlier. The edges of these polygons are parts of the perpendicular bisectors.
- Handle Unbounded Regions: In many cases, some Voronoi cells will be unbounded, meaning they extend infinitely in certain directions. These need to be handled based on the specific requirements of the application, possibly by limiting the diagram to a large but finite bounding box.
- Optimization and Clean-up (Optional): Depending on the algorithm used and the specific requirements of the application, additional steps may be taken to optimize the structure of the Voronoi diagram or clean up artifacts from the computational process.

In this scheme, we employ Abaqus CAE for several key tasks: constructing the geometric model, defining material properties, applying boundary conditions, and meshing the model. After these steps, the model's input file can be exported using Abaqus CAE. Subsequently, phase field sets are incorporated into the input file. The resulting input file comprises two types of elements: the built-in coupled temperature-displacement elements and the user-defined elements (UEL) phase field elements. This combination allows for the comprehensive simulation of materials undergoing both physical displacements and phase changes.

The phase field simulation is carried out with Abaqus and its UEL in a two-tiered approach. Initially, Abaqus and the USDFLD subroutine tackle coupled temperature-displacement issues using the built-in solver. Then, the UEL subroutine calculates damage at material points based on historical energy data and determines the phase field value, which is then fed back to the initial layer. This iterative process facilitates the degradation of material properties and the evolution of the phase field. As a result of this approach, the simulation outputs the stress-strain response and phase field values for thermoelastic solids, revealing the mechanical and fracture characteristics of studied materials. The scheme of phase field simulation of thermo-elasto-damage is shown in Fig. 5.

6. Numerical discussions

6.1. Crack propagation in TGV interconnect structures

Fig. 6a and b illustrate a cross-sectional view and the geometric parameters and boundary conditions of the considered TGV model. In this model, the thickness of the glass interlayer is 230 μm, and the diameters of the internal and external openings of the through hole are 25

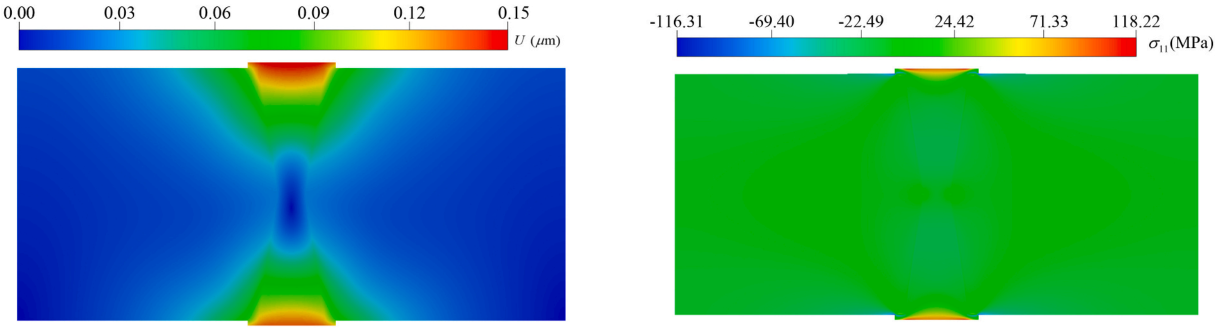

(a) Displacement U

(b) Stress σ_{11}

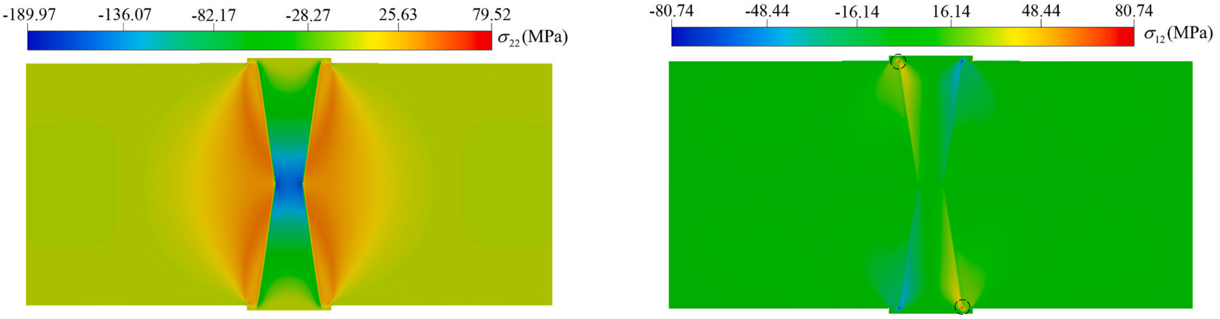

(c) Stress σ_{22}

(d) Stress σ_{12}

Fig. 9. Contours obtained by the present method when the temperature is 125 °C.

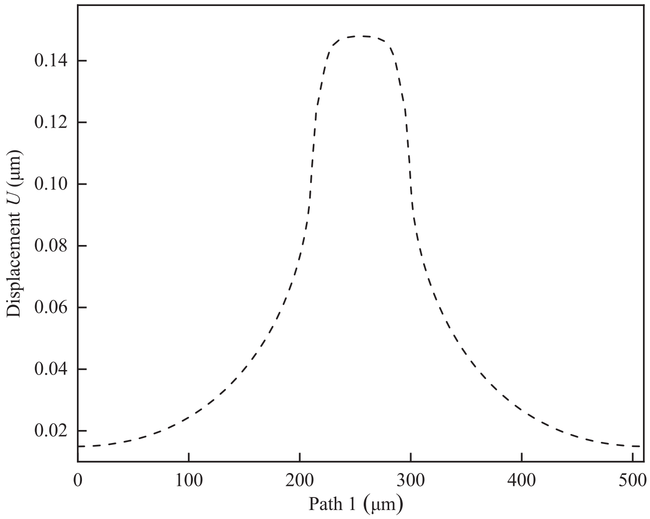

Fig. 10. Displacements U along the path 1 (red dashed curve shown in Fig. 6b). (For interpretation of the references to colour in this figure legend, the reader is referred to the web version of this article.)

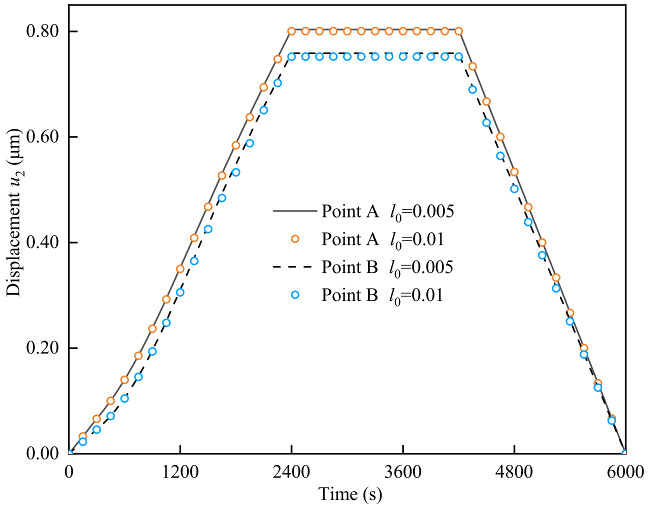

Fig. 11. Displacement u_2 at points A and B influenced by the values of l_0.

μm and 60 μm, respectively. Unless specified otherwise, the unit of all geometric dimensions mentioned in this paper is μm. For ease of description, the filled Cu in TGV will be referred to as TGV-Cu hereafter. As shown in Fig. 6b, the interface between TGV-Cu and glass is set to be fully bonded (ignoring friction). Symmetrical boundary conditions are applied to the left and right surfaces of the glass matrix, and the lower left corner node is fixed in all directions to prevent rigid body movement. Unless specifically stated in this paper, room temperature is considered to be 25 °C, at which temperature all components are in a stress-free state.

The material properties used in the finite element model are listed in Table 1 [37,38], and the mesh is as illustrated in Fig. 7. To more accurately capture the path of crack propagation, the mesh near the area where the crack may extend is refined to a size of 0.001 mm. The mesh contains 46,687 UEL quadrilateral elements and 46,687 coupled temperature-displacement quadrilateral elements. The model is subjected to a loading curve as shown in Fig. 8. The temperature starts increasing from 25 °C at a heating rate of 10 °C/min. After 2400 s of heating, the temperature is maintained at 400 °C for 1600 s, and then it is cooled at a rate of 13.3 °C/min until it reaches room temperature. It should be noted that the time increment Δt for the calculation in this case is 0.25 min. The crack length scale l_0 is 0.005, satisfying the relationship between mesh size and crack length scale as required in literature [17]: the crack length scale is greater than twice the minimum mesh size.

At present, most researchers and engineers analyze TGV issues primarily by calculating stress and displacement at the contact interface to assess potential damage. Fig. 9 also presents the contours of

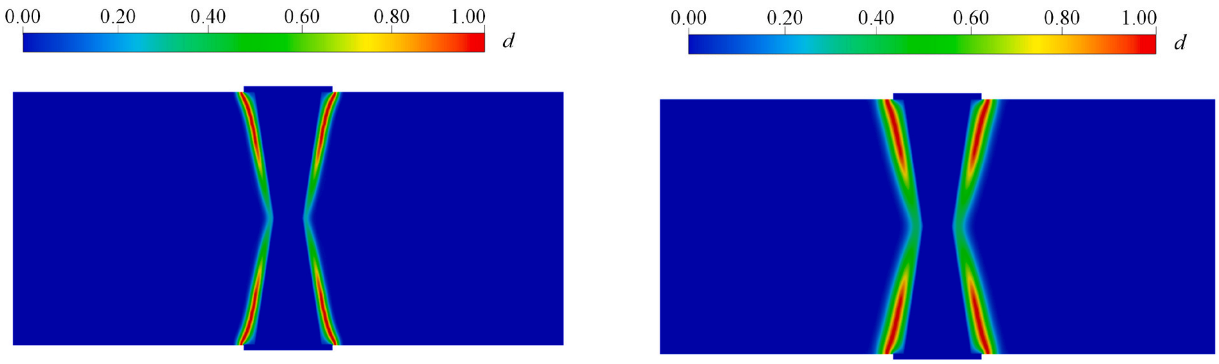

(a) $l_0 = 0.005$

(b) $l_0 = 0.01$

Fig. 12. Crack paths at different length scale parameters.

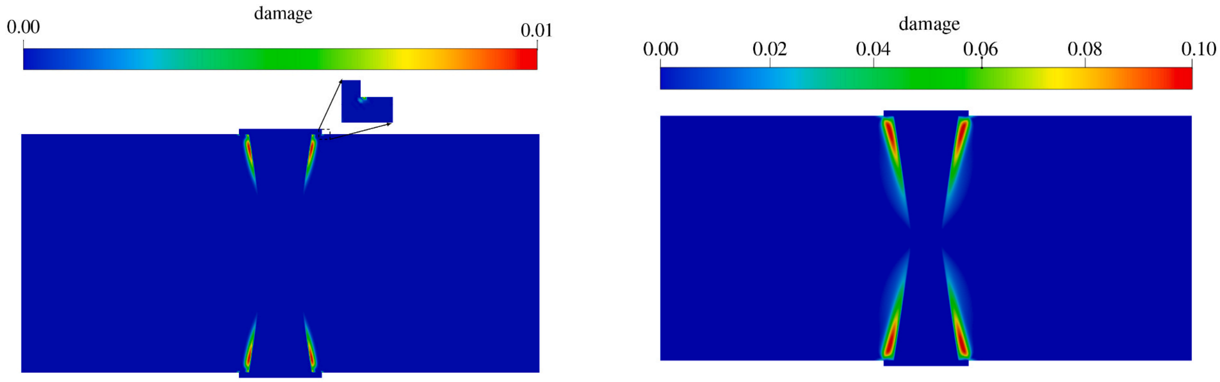

(a) t=405 s and temperature is 92.5 °C

(b) t=735 s and temperature is 147.5 °C

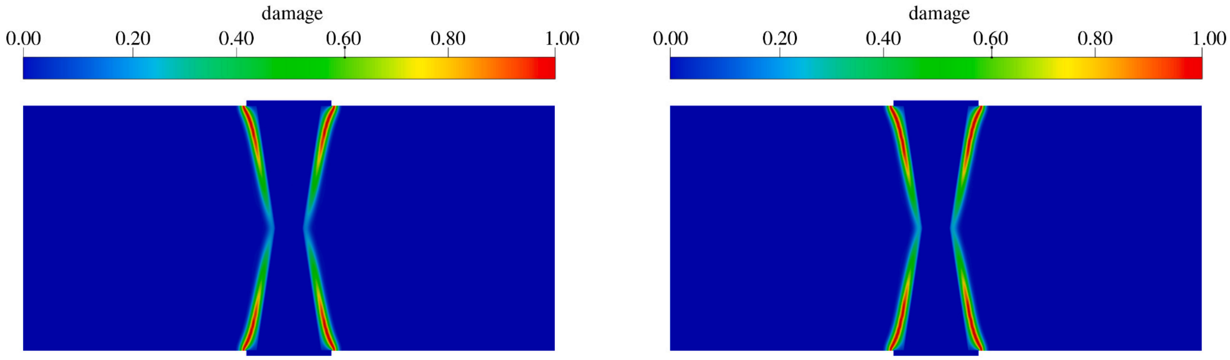

(c) t=2055 s and temperature is 367.5 °C

(d) t=6000 s and temperature drops to 25 °C

Fig. 13. Fracture pattern predicted by the proposed model at different loading stages.

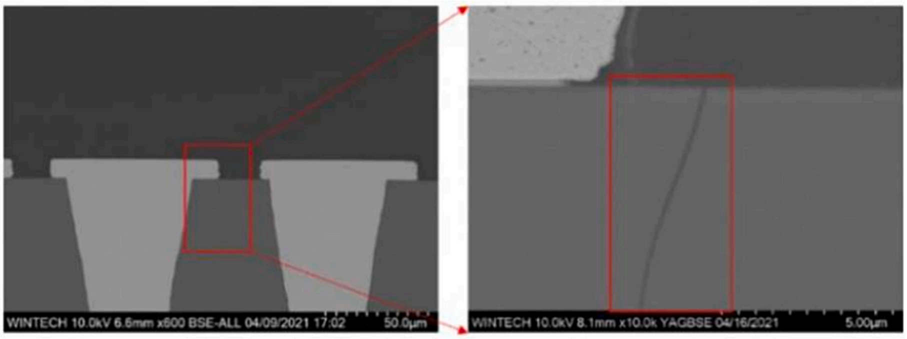

Fig. 14. The pattern of micro-crack observed during the experimental process[39].

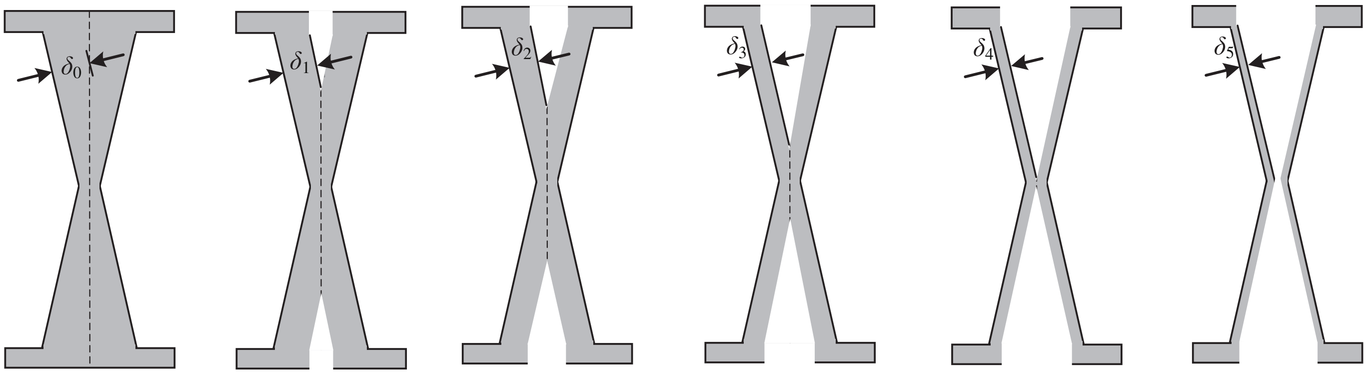

Fig. 15. TGV-Cu structures with different copper wall thicknesses δ_i, $i = 0,1,\dots,5$. δ_0 is a fully copper-filled model. From δ_1 to δ_5, their thicknesses are 27.5 μm, 22.5 μm, 17.5 μm, 12.5 μm, and 7.5 μm, respectively.

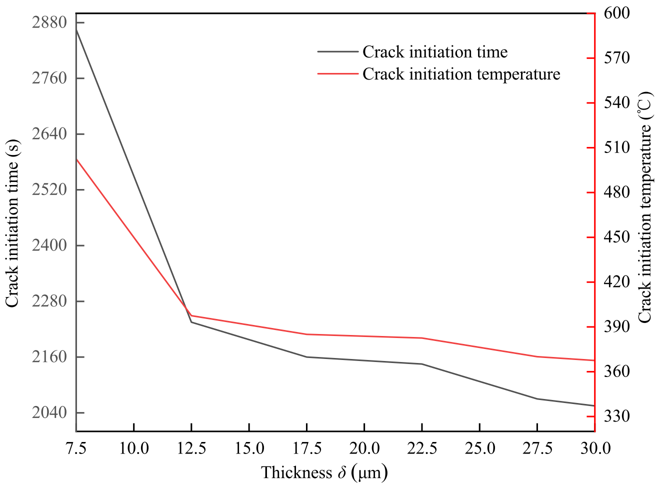

Fig. 16. Crack initiation time and temperature for different copper wall thicknesses δ.

displacement and stresses for the TGV and the substrate when the temperature rises to 125 °C. Fig. 9a shows the displacement cloud diagram of the model. The maximum expansion of TGV-Cu at the top and bottom reaches 0.15 μm, which is one of the significant reasons for the failure of the TGV interconnect structure. Displacements along the top surface, represented by path 1 (depicted as a red dashed curve in Fig. 6b) are presented in Fig. 10. As shown in Fig. 9b and c, the expansion of copper results in the glass being subjected to radial compression and axial tension, respectively. Furthermore, in Fig. 9d, extreme values of shear stress appear at the upper and lower corner surfaces (domains inside the black dashed circle) of the TGV through-hole. This is one of the main causes of cracking in the glass substrate and may also lead to cracking at the interface between TGV-Cu and glass.

To verify the sensitivity of the used phase field model to the parameter l_0, two points A and B (shown in Fig. 6b) are selected for analysis. Fig. 11 presents the displacements at points A and B over time when l_0 is set to 0.01 and 0.005, respectively. From the figure, it can be observed that the displacements are minimally affected by variations in l_0, highlighting the advantage of the adopted phase field model: its low dependency on the parameter l_0. Fig. 12a and b show the final crack evolution paths obtained using various internal length scales l_0. The crack diffusion width does not affect the final crack evolution state, with

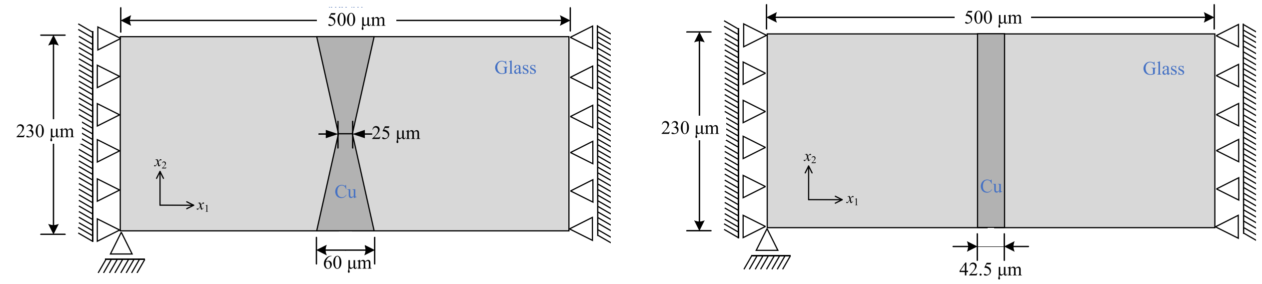

(a) Double trapezoidal via

(b) Vertical via

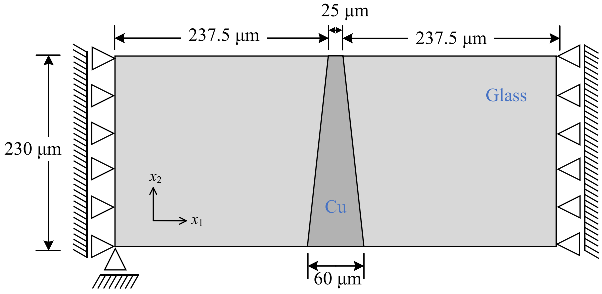

(c) Single trapezoidal via

Fig. 17. TGV with different through-hole shapes.

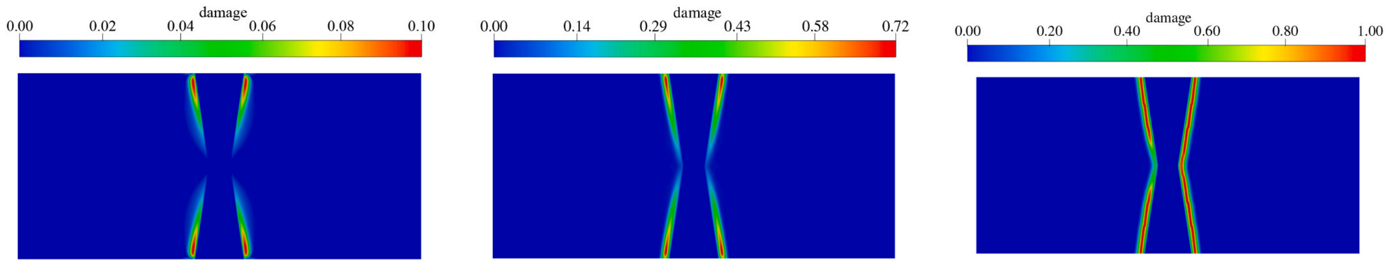

(a) $t = 720$ s (b) $t = 1440$ s (c) $t = 4800$ s

Fig. 18. Fracture pattern predicted by the proposed model at different loading stages for double trapezoidal via.

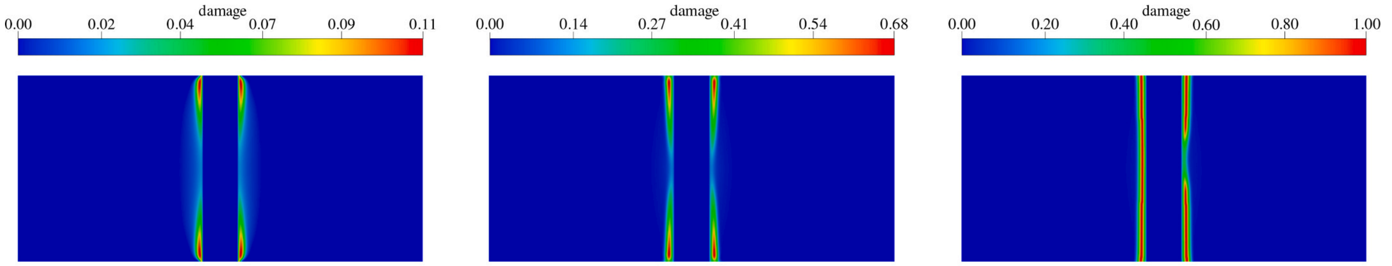

(a) $t = 720$ s (b) $t = 1440$ s (c) $t = 4800$ s

Fig. 19. Fracture pattern predicted by the proposed model at different loading stages for vertical via.

the centerline of the localized damage zone representing the actual crack development path. For l_0 values of 0.005 mm and 0.01 mm, the modeled crack initiation times are 2040 s and 1995 s, respectively. This small difference in initiation times demonstrates that the adopted phase-field analysis model is relatively insensitive to changes in the l_0 parameter.

Actually, merely analyzing the stress in the TGV structure does not suffice to determine the damage domain and failure path of the structure. That's the reason why we propose the phase field model to analyze the failure of this structure. As shown in Fig. 13a, when the temperature increases to 92.5 °C, damage first occurs on the upper and lower side walls of the interface between TGV-Cu and the glass substrate. From the magnified section of Fig. 13a, we can find that damage is also observed at the edge of the RDL layer. As the temperature further rises to 147.5 °C, the damaged area expands, showing a tendency to extend towards the edge of the RDL layer. When the temperature reaches 367.5 °C, the crack damage value d hits 1.00, and the crack begins to propagate, forming surface micro-cracks along the sidewall of the TGV as shown in Fig. 13d. It should be noted that Fig. 13d presents the final results after the temperature has returned to room temperature 25 °C. This is similar to the crack propagation path observed by Zhao et al. [39] in their experiments. (See Fig. 14.)

6.2. The impact of copper thickness on crack formation in TGV

Here, we will study the impact of varying copper thickness δ on the reliability of TGV structures, where the δ denotes the thickness of copper adhering to the inner walls of the through-hole, as depicted in Fig. 15. Here, six models with copper wall thicknesses of δ_0 to δ_5 are examined, with δ_0 being 30 μm representing a fully copper-filled model. From δ_1 to δ_5, their thicknesses are 27.5 μm, 22.5 μm, 17.5 μm, 12.5 μm, and 7.5 μm, respectively. For the δ_5 case, the hole is a through-hole, and only a layer of copper is adhered to the walls of the TGV.

In the numerical analysis, all the models are subjected to a heating rate of 10 °C/min, with an ambient temperature of 25 °C. The time increment, mesh division strategy, and length scale l_0 are consistent with those mentioned in section 6.1. The temperature corresponding to the phase field damage value $d = 1.00$ is designated as the crack initiation temperature, and the corresponding time is defined as the crack initiation time. Fig. 16 illustrates the crack initiation temperatures and times for varying copper wall thicknesses δ. It is observed that reducing the thickness of copper increases both the crack initiation temperature and time. Notably, when the copper thickness is δ_5, the copper walls on both sides of the TGV separate (shown in Fig. 15), significantly raising both the crack initiation temperature and time. The results indicate that reducing the thickness of TGV-Cu is a key factor in enhancing the

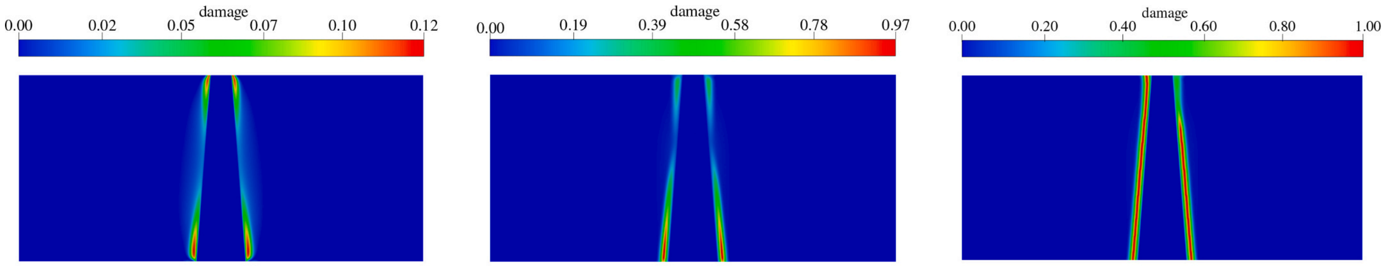

(a) $t = 720$ s (b) $t = 1440$ s (c) $t = 4800$ s

Fig. 20. Fracture pattern predicted by the proposed model at different loading stages for single trapezoidal via.

Table 2
Crack initiation temperature and time for TGVs with different through-hole shapes.

Shapes of through-hole	Double trapezoidal	Vertical	Single trapezoidal
Crack initiation temperature (s)	2565	1995	1515
Crack initiation time (°C)	452.5	357.5	277.5

reliability of interconnect structures during use. However, it's important to note that this analysis neglects the direct strength implications resulting from this thickness reduction. Previous research has also shown that the mechanical properties of TGV-Cu are sensitive to temperature variations (from room temperature to 400 °C) [30]. Future work should focus on exploring the relationship between these factors and their impact on the overall reliability of the structure.

6.3. *The impact of TGV through-hole shape on reliability*

Influenced by via formation technologies, TGV through-hole shapes vary, mainly including: double trapezoidal via, vertical via, and single trapezoidal via. Due to the significant difference in the thermal expansion coefficients between copper and glass, thermal stress during subsequent process steps can cause interface delamination or substrate cracking, thereby directly impacting reliability. Therefore, investigating the impact of through-hole shape on TGV structure is of significant importance. As shown in Fig. 17, models of three different through-hole shapes are established, with the area of TGV-Cu in each model being the same, at 9775 μm^2. A global heating rate of 10 °C/min and an ambient temperature of 25 °C are applied, with other variables being the same as in Section 6.1.

Figs. 18, 19 and 20 present the fracture pattern predicted by the proposed model at different loading stages for TGVs with different through-hole shapes. As shown in Figs. 18a, 19a and 20a, when the temperature reaches 145 °C ($t = 720$ s), damage begins to occur in the glass substrate, with the primary damage in the TGV structures of the three models concentrated at the sidewalls of the upper and lower openings. As illustrated in Figs. 18b, 19b and 20b, as the temperature further increases to 265 °C ($t = 1440$ s), the damage within the glass substrate extends further. It is observable that the damage of the single trapezoidal via is mainly concentrated on the sidewalls at both sides of the lower base of the trapezoid. As the temperature continues to rise, cracks begin to propagate (when the damage value reaches 1), ultimately forming the crack morphology shown in Figs. 18c, 19c and 20c. The cracks in both double trapezoidal and vertical vias extend inward from the sidewalls of the openings at both ends, whereas the cracks in the single trapezoidal via propagate upwards from the lower base towards the upper base.

By comparing the crack initiation times and temperatures of TGV interconnect structures with three different through-hole shapes (listed in Table 2), it is found that under the same volume of filled copper, double trapezoidal via perform better than vertical via, with single trapezoidal via being the least favorable. It is important to note that the crack initiation time for the double trapezoidal via with the RDL layer is

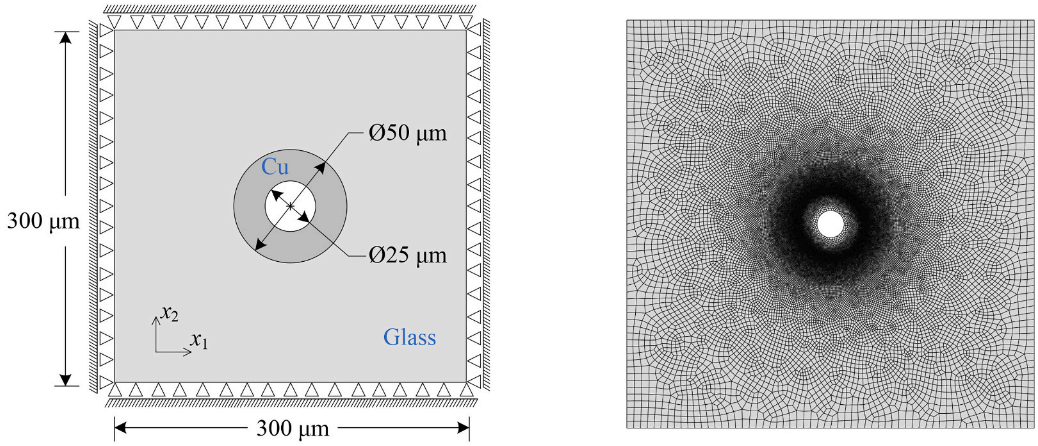

(a) Boundary conditions and geometric parameters

(b) Mesh used in the numerical model

Fig. 21. Parameters and mesh used in the TGV model.

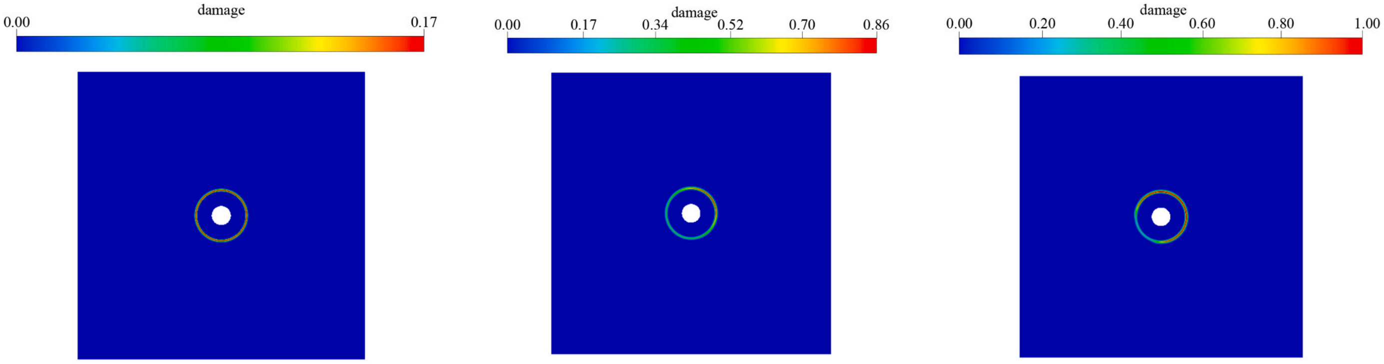

(a) $t = 600$ s

(b) $t = 960$ s

(c) $t = 2250$ s

Fig. 22. Fracture pattern predicted by the proposed model at different loading stages.

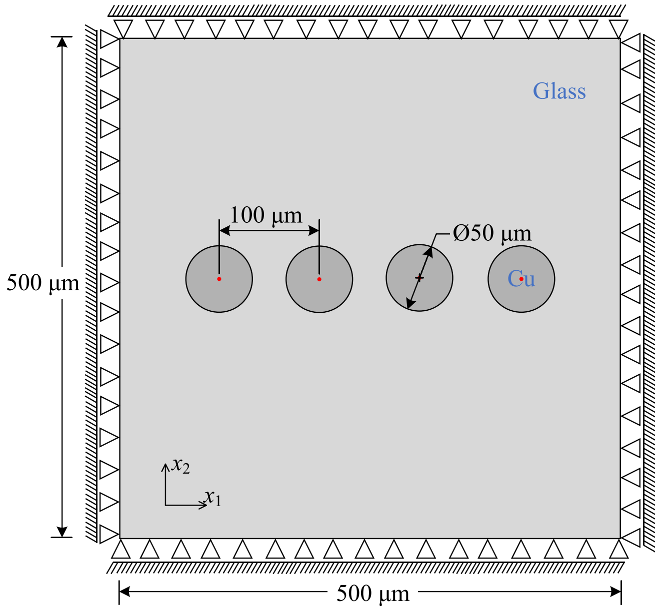

Fig. 23. Boundary conditions and geometric parameters of considered model for the heating stage.

2055 s (given in Fig. 16), whereas it is 2565 s for the double trapezoidal TGV via without the RDL layer. This indicates that the inclusion of the RDL layer exacerbates the damage to the TGV via.

6.4. Circumferential and radial cracks simulation in TGV structure

TGVs experience thermo-mechanically induced failure modes, primarily attributed to the mismatch in material properties, particularly the coefficient of thermal expansion, between the glass substrate and Cu. There are two distinct types of thermo-mechanically induced crack systems in the TGV substrate: radial and circumferential cracks. Radial cracks emerge during the heating stage of an annealing cycle, whereas circumferential cracks develop during the cooling phase.

6.4.1. Circumferential cracks during the cooling process

To validate the effectiveness of the proposed numerical scheme, we will conduct tests and analysis on the crack patterns mentioned in literature [40] by using the phase field method. The FE model and mesh are as shown in Fig. 21a and b, respectively. As shown in Fig. 21a, all edges of the model are subjected to symmetrical boundary conditions. The temperature load decreases from 400 °C to room temperature (25 °C), with all structures being in a zero-stress state at 400 °C. The cooling rate is set to 10 °C/min, with each time increment Δt being 0.25 min. To better capture the cracks, the mesh around the Cu is refined, with a mesh size of 0.001 mm. The crack length scale l_0 is 0.0015, the fracture energy G_c is 3 N/m, and the critical shear ratio χ is 1.0×10^5, to simulate the cooling-induced crack propagation in TGV through-holes.

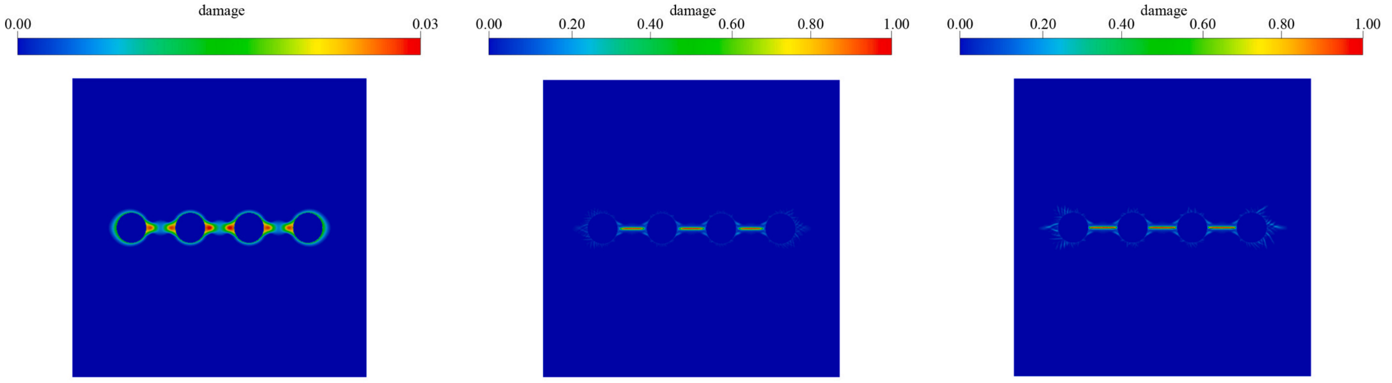

(a) $t = 1080$ s (b) $t = 2160$ s (c) $t = 2760$ s

Fig. 24. Fracture pattern predicted by the proposed model at different loading stages for heating stage.

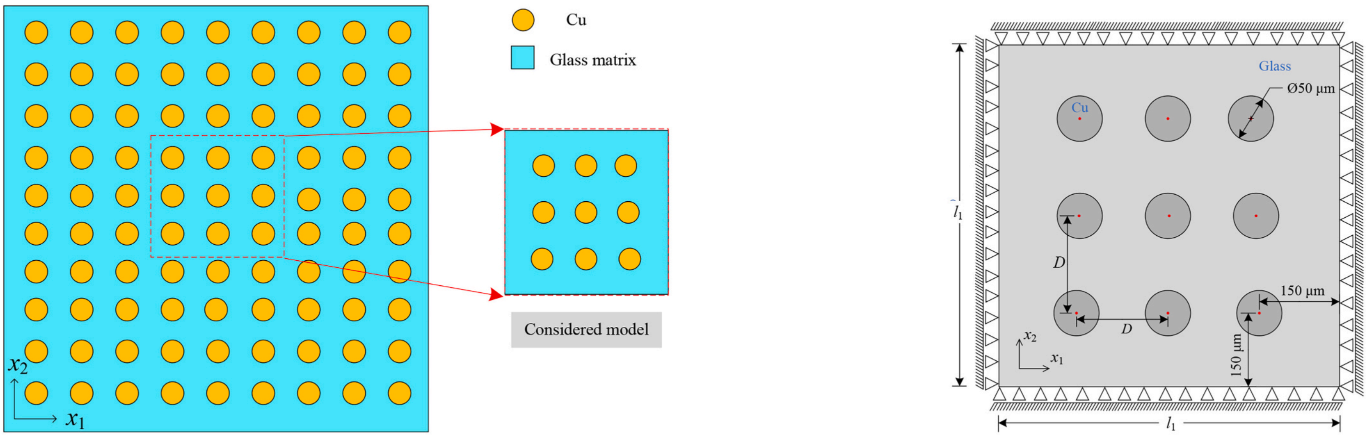

(a) Position relationship of the TGVs. (b) The computed model

Fig. 25. Schematic diagram of the TGV architecture used in this study.

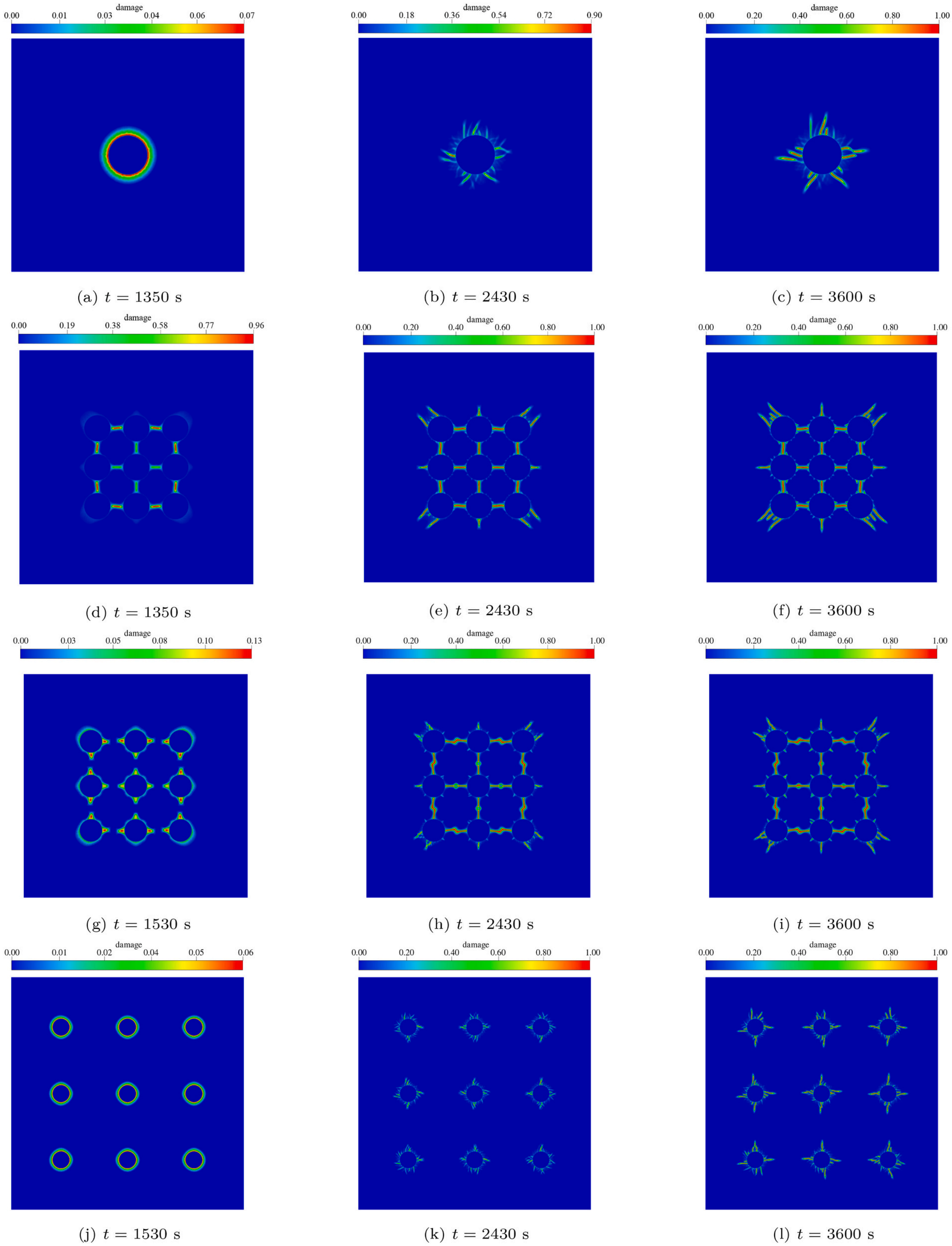

(a) $t = 1350$ s (b) $t = 2430$ s (c) $t = 3600$ s

(d) $t = 1350$ s (e) $t = 2430$ s (f) $t = 3600$ s

(g) $t = 1530$ s (h) $t = 2430$ s (i) $t = 3600$ s

(j) $t = 1530$ s (k) $t = 2430$ s (l) $t = 3600$ s

Fig. 26. Fracture pattern predicted by the proposed model at different loading stages: (a)-(c) in the case only one TGV ($D = 0\mu$m); (d)-(f) $D = 75$ μm; (g)-(i) $D = 100\mu$m; (j)-(l) $D = 200\mu$m.

When the TGV through-hole is subjected to a cooling load, the difference in thermal expansion coefficients between TGV-Cu and the Glass substrate causes the glass substrate to experience tensile stress. This results in the formation of a circumferential damage zone at the edge of the glass substrate, as shown in Fig. 22a and b. As the temperature further decreases, the damage progresses and eventually leads to the formation of circumferential cracks as shown in Fig. 22c. The conclusions of this case are consistent with the experimental findings in literature [40], indicating that the proposed scheme can effectively simulate TGV failure issues.

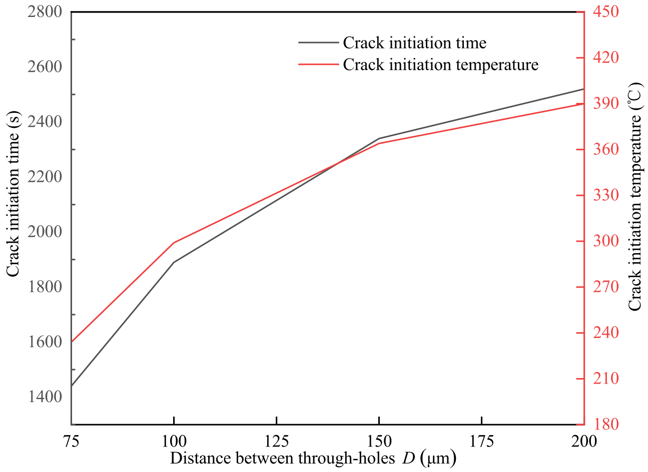

Fig. 27. Initiation time and temperature of cracking corresponding to different TGV distance *D*.

6.4.2. Radial cracks during the heating stage

Under heating load, the TGV structures witness radial cracks as shown in the reference [41]. Here, we will analyze the crack patterns utilizing the proposed phase field method. The computational model is given in Fig. 23, with all edges of the model subjected to symmetrical boundary conditions. The annealing profile having constant heating rates 8.7 °C/min which varied from 25 °C to 425 °C. Here, the time increment $\Delta t = 1.5$ min and the remaining parameters are consistent with those in Section 6.4.1.

Fig. 24 illustrates the fracture pattern predicted by the proposed model at different loading stages during the heating phase. In this phase, the expansion of Cu, which has a higher CTE, is constrained by the surrounding glass substrate, leading to stress accumulation within the model. This stress induces tensile stress in the circumferential direction, and damage in the TGV structure initially manifests at the interface between the glass substrate and TGV-Cu, as depicted in Fig. 24a. As the temperature continues to rise, the area of damage further expands, ultimately resulting in the condition depicted in Fig. 24b and c, where radial cracks are formed. The conclusions of this numerical example are consistent with the experimental findings in literature [41].

6.4.3. The impact of TGV-Cu spacing on crack propagation in the glass matrix

For packaging structures based on glass vias, the distance between the vias can influence the crack patterns in the packaging structure. Here, we will study the impact of the spacing between glass vias on the crack patterns in TGV packaging structures by using the model given in Fig. 25. Fig. 25a gives the distribution of TGV in the computational model. In this part, a model with 3 × 3 circular TGVs with diameter = 50 μm is considered. The distance from the center of the outermost TGV to the edge of the model is fix at 150 μm. The spacing between two TGVs is denoted by *D*. The ambient temperature is set at 25 °C, with a heating load of 8.7 °C/min applied. The other conditions are consistent with those in section 6.4.2.

Fracture pattern of TGVs with 4 different distance values 0 μm, 75 μm, 100 μm and 200 μm is compared in Fig. 26. Figs. 26a-26c show the crack pattern of the model when there is only one TGV ($D = 0\mu$m). The cracks radiate from the TGV interface and spread outward. The interaction between TGVs and the crack pattern inside the model becomes apparent in cases where $D \neq 0\mu$m (from Fig. 26d to 26l). As the distance *D* between the TGVs increases, the interaction between the cracks decreases. When $D = 200\mu$m, it can be observed from Figs. 26j-26l that the interaction disappears. Fig. 27 presents the initiation time and temperature of cracking corresponding to different TGV spacings. From this figure, it can be observed that as the distance between the through holes continually increases, the initiation time and the initiation temperature for the cracks gradually increase.

6.5. Crack propagation in TSV interconnect structures

Fig. 28 presents a schematic of a TSV interposer, primarily consisting of a Si substrate, SiO_2 insulation layer, diffusion barrier layer (usually TiW, TiN, or Ta), and filled Cu supporting electrical connections. For convenience in the following text, the filled Cu in the TSV will be

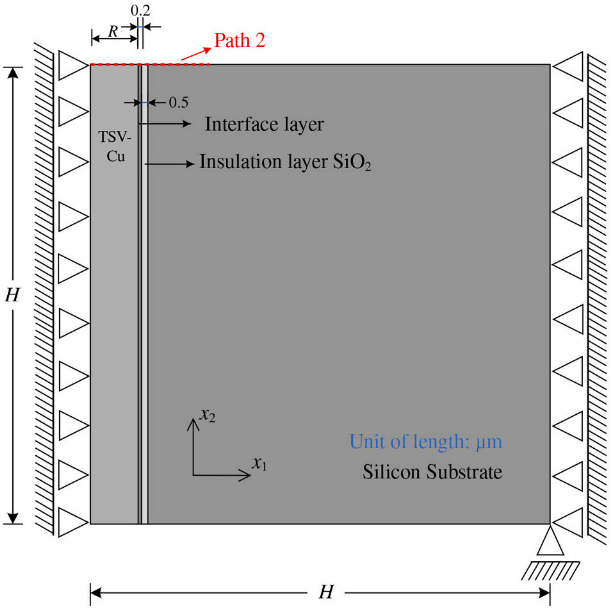

Fig. 29. TSV computational model.

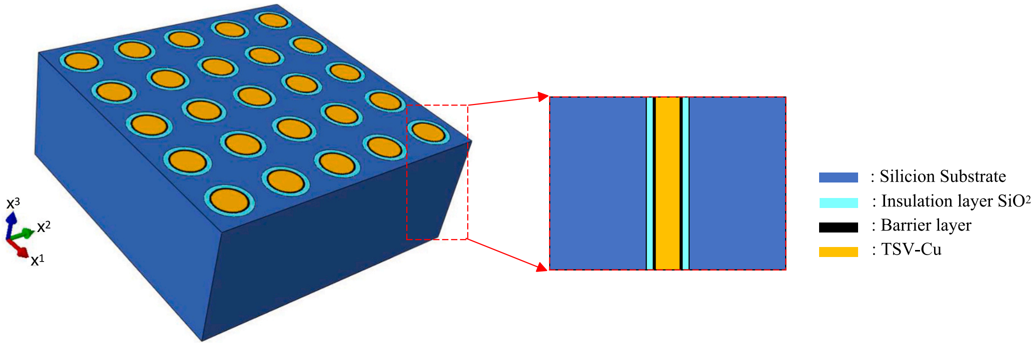

Fig. 28. Schematic of a TSV interposer.

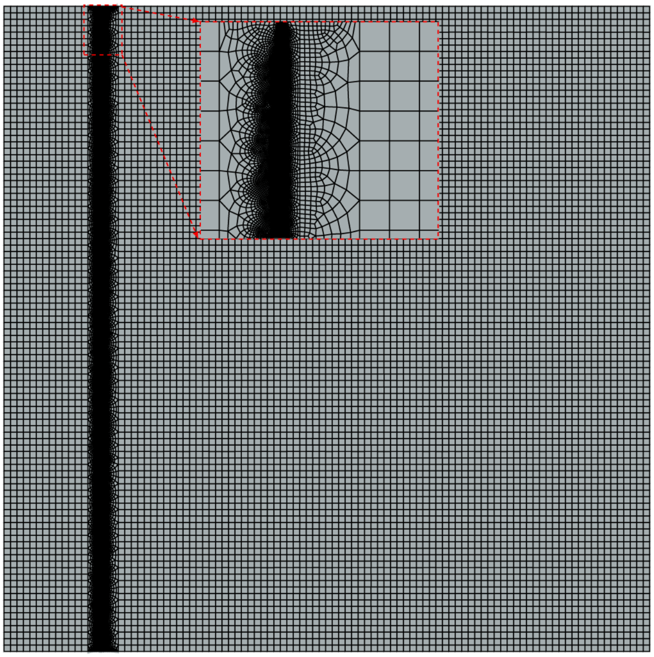

Fig. 30. Mesh used in the numerical model.

Table 3
Material parameters relevant to the TSV structure.

Material	Si	Glass	Cu	Interface layer
Young's modulus E (GPa)	130.00	77.80	128.00	77.80
Poisson's ratio v	0.28	0.17	0.30	0.17
Density ρ (kg/m^3)	2330	2200	8960	2200
Thermal conductivity coefficient (W m^{-1} K^{-1})	130.00	1.53	393.50	1.53
Specific heat capacity (J kg^{-1} K^{-1})	700	600	386	600
Thermal expansion coefficient α_0 (ppm/°C)	2.80	0.48	17.00	0.48
Tensile strength (MPa)	1600	50	209	40
Fracture toughness (N/m)	3.0	8.0	690.3	3.2
Critical shear ratio χ	0.05	0.6	1.0	0.6

referred to as TSV-Cu. The material of the TSV interconnect structure exhibits significant differences in the coefficient of thermal expansion (CTE). Specifically, the CTE of TSV-Cu is 17.0 ppm/°C, while the CTE of the Si substrate is 2.8 ppm/°C, meaning the CTE of TSV-Cu is nearly 6 times that of Si. The CTE of TSV-Cu also differs substantially from that of SiO_2 and the barrier layer, with the insulation layer SiO_2 having a CTE of 0.48 ppm/°C and the barrier layers (Ti, Ta, TiW) having CTEs in the range of approximately 1 to 6 ppm/°C [42]. The circuit layer of the TSV interconnect is on the micro to nanometer scale, while the diameter of the TSV-Cu is several tens of micrometers, and its depth can even reach a hundred or two hundred micrometers. In the fabrication process of the interconnect structure, the TSV structure involves multiple temperature loads in the range of 200–450 °C. The significant temperature difference during the fabrication process can cause substantial expansion or contraction in the volume of TSV-Cu, leading to failure modes such as deformation, delamination, or fracture of the circuit layer above it. Here, we will utilize the phase-field model proposed in this paper to investigate the failure behavior of the TSV interconnect structure.

6.5.1. *TSV-Cu protrusion*

Fig. 29 shows the computational TSV model. To simplify the computational model, the influence of the thinner barrier layer is ignored. The thickness of the SiO_2 layer is 0.5 μm. A 0.2 μm thick interfacial layer is inserted between TSV-Cu and SiO_2 to characterize the bonding behavior at the interface between TSV-Cu and SiO_2. The interface layer is assigned properties according to those of SiO_2, with the difference being in its fracture energy and tensile strength. The left and right boundaries of the model are set to symmetrical boundary conditions, and the bottom right corner of the model are fixed. The model applies a heating condition of 10 °C/min to simulate the annealing process of the TSV structure, with a time increment step of 0.25 min. The mesh used in the computation is shown in Fig. 30, with a refined mesh at the TSV interface. The element size of the interface layer is 0.00003 mm, and the crack length scale l_0 is 0.00015 mm. When $\mathrm{H} = 100\ \mu$m and $R =$ 15 μm, the model contains 114,442 UEL quadrilateral elements and 114,442 coupled temperature-displacement quadrilateral elements. To facilitate the description of the relationship between TSV size and reliability, an aspect ratio of the TSV structure is defined here as the ratio of the height H of TSV to the diameter R of TSV-Cu ($H/2R$). The material parameters used for the numerical calculations are presented in Table 3 [42–46].

When the TSV structure is annealed and heated to 125 °C, the displacement distribution of the TSV are as shown in Fig. 31. As can be observed from Fig. 31a, significant expansion occurs in TSV-Cu, which is primarily caused by the mismatch in the CTE between TSV-Cu, Si, and SiO_2. From Fig. 31b, it is observed that radial compressive stress occurs at the top of the SiO_2 insulation layer. Additionally, in Fig. 31c and d, due to the protrusion of TSV-Cu under the heating load, significant tensile and shear stresses are generated in the SiO_2 insulation layer and the silicon substrate. At the same time, shear stress peaks are formed near the top of the SiO_2 insulation layer and TSV-Cu.

To further explore how the size of TSV-Cu in TSVs influences its protrusion behavior, the following sections will investigate the effects from different perspectives, specifically focusing on the radius R and the height H of TSV-Cu, to discern the patterns of how these dimensions affect TSV protrusion.

6.5.2. *The impact of radius R on the protrusion of TSV-Cu*

With H fixed at 100 μm, the values of R are 2.5 μm, 5 μm 10 μm, 15 μm, 20 μm, and 25 μm, respectively. Fig. 32 shows the protrusion height of TSV along path 2 when the temperature is 425 °C. As can be observed from Fig. 32, the protrusion of TSV-Cu takes a shape that is lower in the middle and higher at both ends. With the increase of radius R, the height of the protrusion also continually increases. From Fig. 33, it can be seen that as the aspect ratio increases, the maximum protrusion of TSV gradually decreases. When the aspect ratio exceeds 4, the change in protrusion amount significantly diminishes. Thus, it can be concluded that when the height H of TSV-Cu is fixed, the amount of protrusion is not directly proportional to the aspect ratio of the TSV structure. Fig. 34 shows us the initiation time and initiation temperature of cracking in the interface layer under different aspect ratios. As can be seen from the Fig. 34, the larger the aspect ratio, the higher the initiation time and initiation temperature for cracking in the TSV structure. When the aspect ratio exceeds 4, the growth trend significantly decreases.

6.5.3. *The impact of height H on the protrusion of TSV-Cu*

In this section, the protrusion behavior of TSV-Cu is investigated by varying the height H. When $R = 15\mu$m, the selected values for H are 30 μm, 50 μm, 75 μm, 100 μm, 125 μm, 150 μm, and 250 μm. Fig. 35 displays the protrusion height of TSV along path 2 at a temperature of 425 °C for various heights H. It can be observed that as the height H increases, the protrusion height of TSV along the path also continuously increases. Fig. 36 presents the protrusion height along the path under different aspect ratios when R is fixed. As the aspect ratio increases, the maximum protrusion of TSV gradually increases. When the radius R of TSV-Cu is fixed, the protrusion amount shows a positive correlation with the aspect ratio of the TSV structure, meaning the higher the height of TSV-Cu, the greater the amount of protrusion. When R is fixed, Fig. 37 illustrates the initiation time and initiation temperature of cracking in

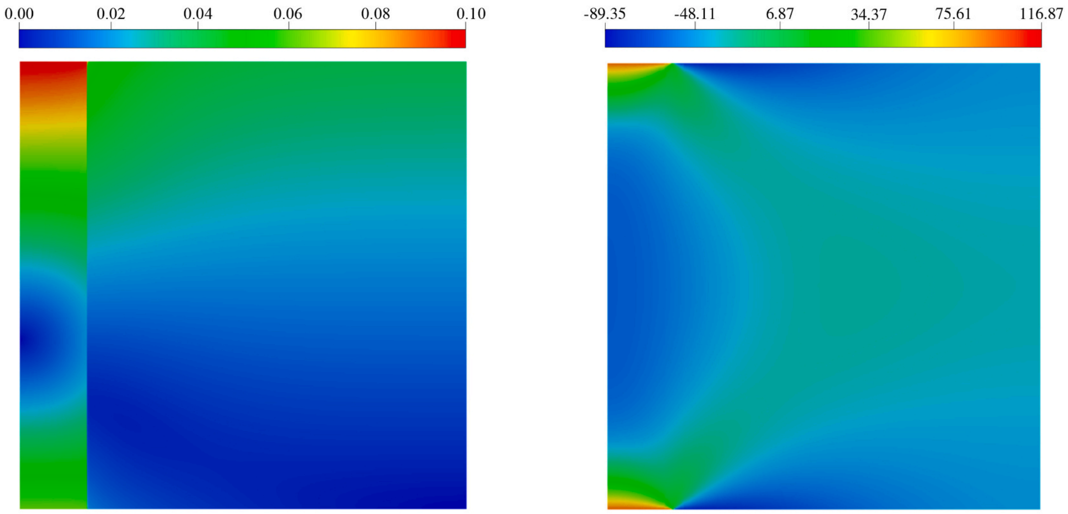

(a) Displacement $U(\mu m)$.

(b) Stress σ_{11} (MPa)

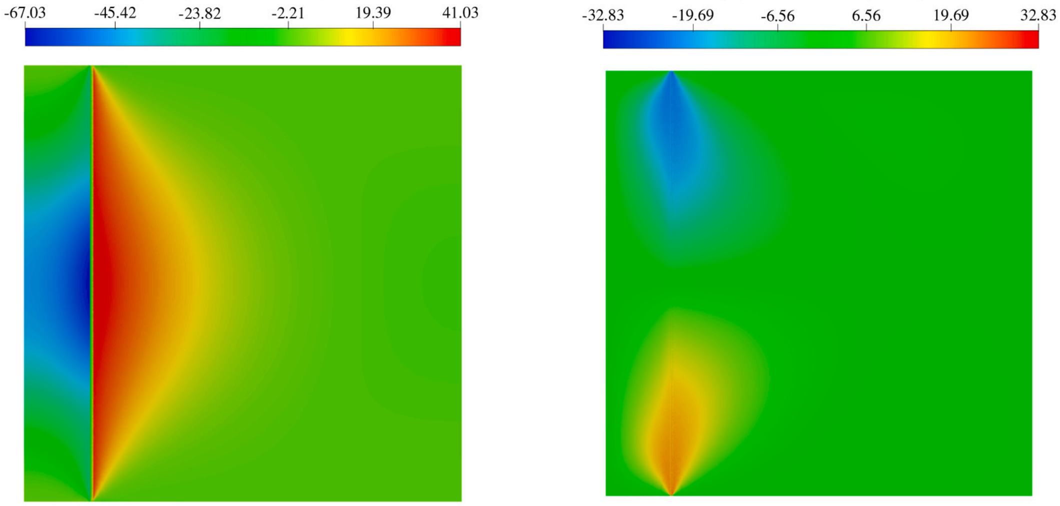

(c) Stress σ_{22} (MPa)

(d) Stress σ_{12} (MPa)

Fig. 31. Displacement and stress distribution during the annealing process.

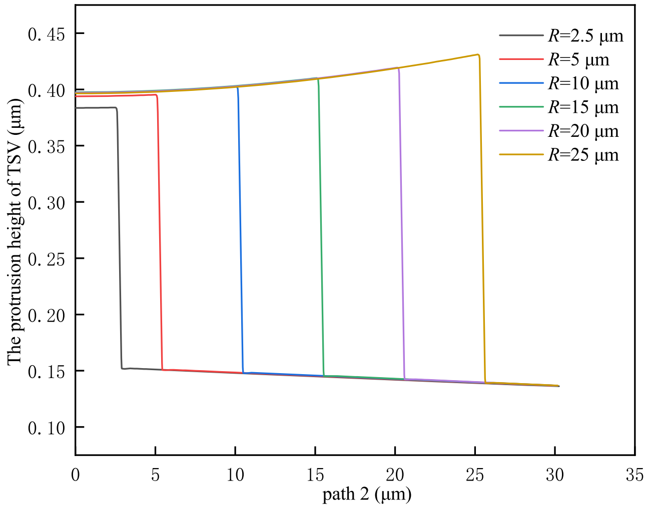

Fig. 32. Protrusion height of TSV-Cu along path 2 for different values of R.

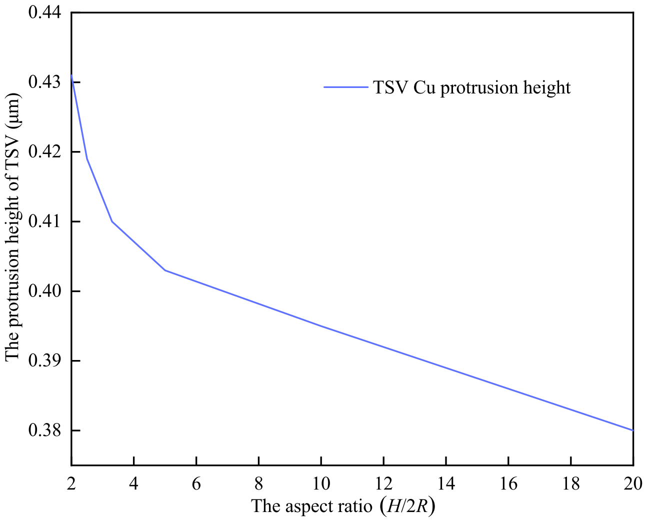

Fig. 33. When H is fixed, protrusion height along the path 2 under different aspect ratios.

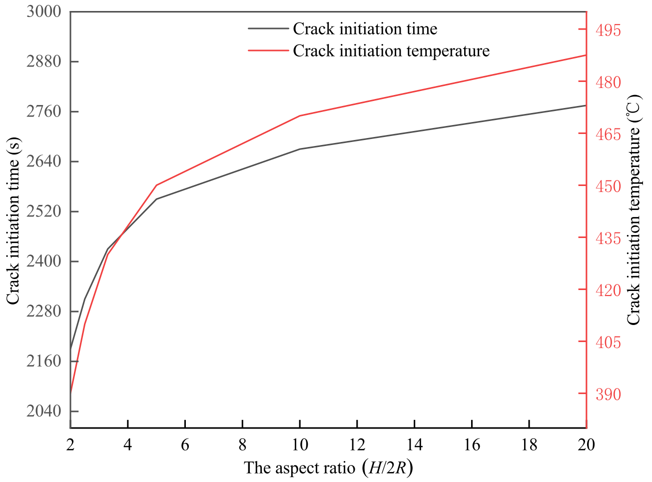

Fig. 34. When H is fixed, the initiation time and temperature of cracking in the interface layer for different aspect ratios.

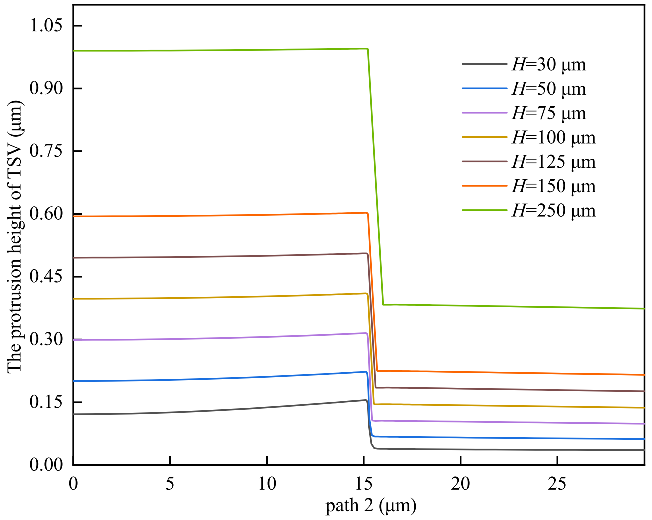

Fig. 35. The protrusion height of TSV-Cu along path 2 for different values of H.

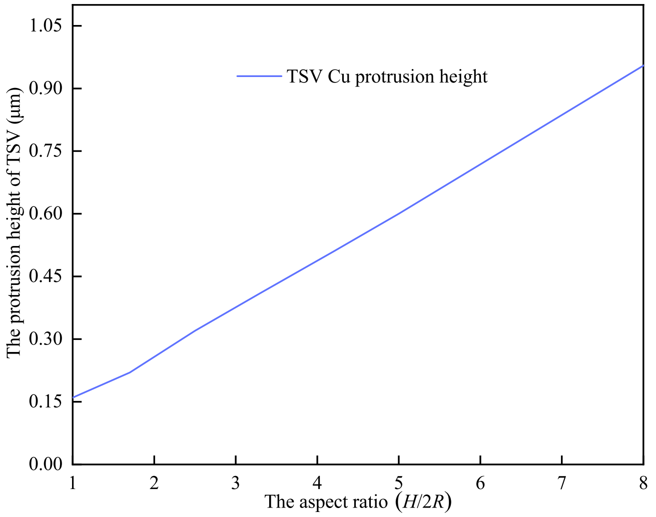

Fig. 36. The protrusion height along the path 2 under different aspect ratios when R is fixed.

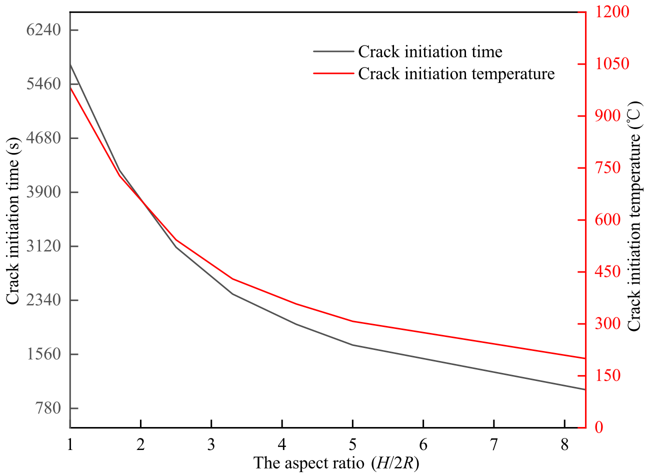

Fig. 37. For a fixed R, the initiation time and temperature of cracking in the interface layer under different aspect ratios.

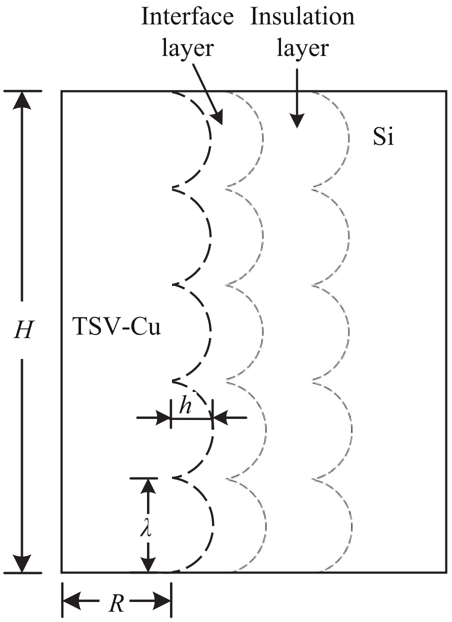

Fig. 38. The model of the TSV interface layer.

the interface layer under different aspect ratios. From Fig. 37, it can also be deduced that the larger the aspect ratio, the smaller the initiation time and initiation temperature for cracking in the TSV structure. When the aspect ratio exceeds 4, the trend of decrease significantly levels off, implying that when R is fixed, the larger the aspect ratio, the weaker the resistance of the interface layer to damage, making the structure more susceptible to failure.

6.5.4. The impact of interface roughness on TSV structure

During the fabrication of TSV, the highly efficient Bosch etching process is commonly used. This process results in the formation of a scallop-like morphology on the TSV walls, characterized by a certain degree of roughness [47]. To analyze the impact of different roughness levels on the cracking of the interface layer, two parameters, λ and h, are selected to quantitatively describe the interface roughness, as shown in Fig. 38. They represent the wavelength and peak amplitude of the scallop-shaped interface, respectively. Hence, the interface roughness can be expressed as h/λ.

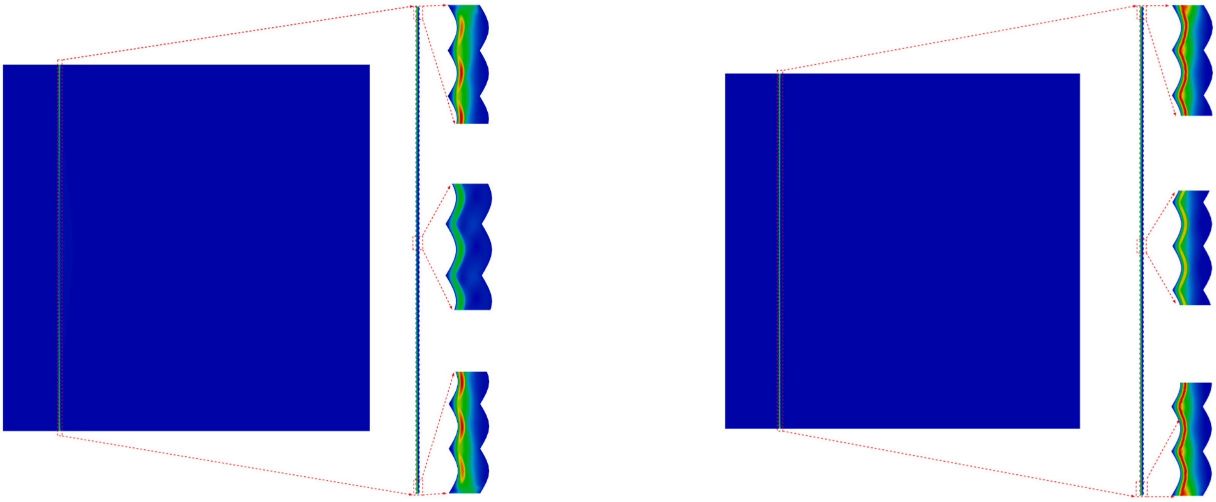

(a) $t = 600$ s

(b) $t = 2400$ s

Fig. 39. Fracture pattern predicted by the proposed model at different loading stages when $h/\lambda = 0.2$.

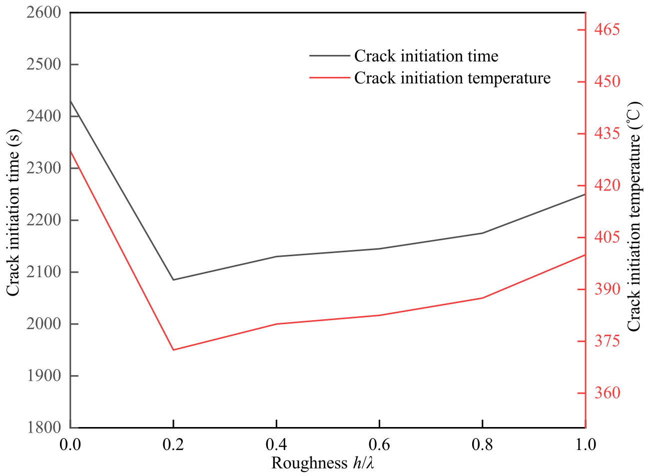

Fig. 40. The initiation time and temperature of the interfacial layer under different interface roughnesses.

To study the impact of different interface roughness levels, 6 different roughness conditions will be considered for analysis. With $H = 100\mu$m and $R = 15\mu$m, the first condition has no roughness, i.e., $\lambda = 100\mu$m and $h = 0\mu$m. For the remaining 5 conditions, $\lambda = 1\mu$m, and h takes values of 0.2μm, 0.4μm, 0.6μm, 0.8μm, and 1.0μm, respectively.

Fig. 39a and b shows us the fracture pattern predicted by the proposed model at different loading stages when $h/\lambda = 0.2$. From Fig. 39a we can find the interface damage is primarily concentrated at the peaks near the top and bottom openings of the model. With further increase in temperature, when $t = 2400$ s, wave-shaped cracks form, as shown in Fig. 39b, which has a morphology similar to the interface cracking observed in the reference [43].

Fig. 40 shows us the initiation time and temperature of the interfacial layer under different interface roughnesses, from which we can find that

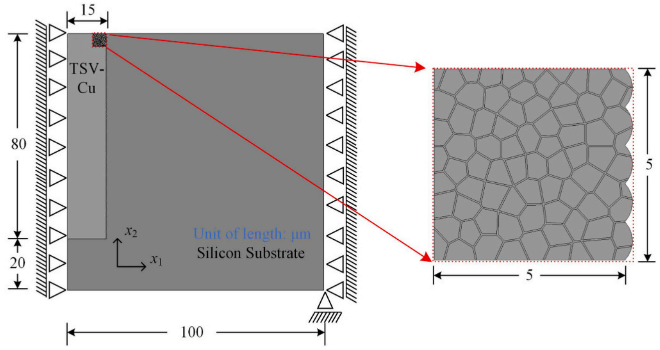

Fig. 42. TSV-Cu seed layer microstructure model.

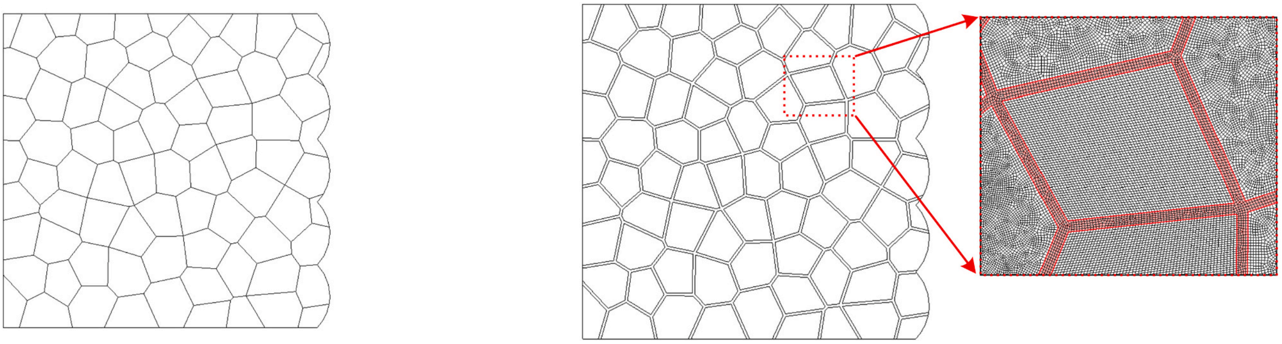

(a) Cu grain boundary

(b) Voronoi polygons with a thick grain boundary and a locally magnified mesh

Fig. 41. Schematic diagram of Voronoi polygons.

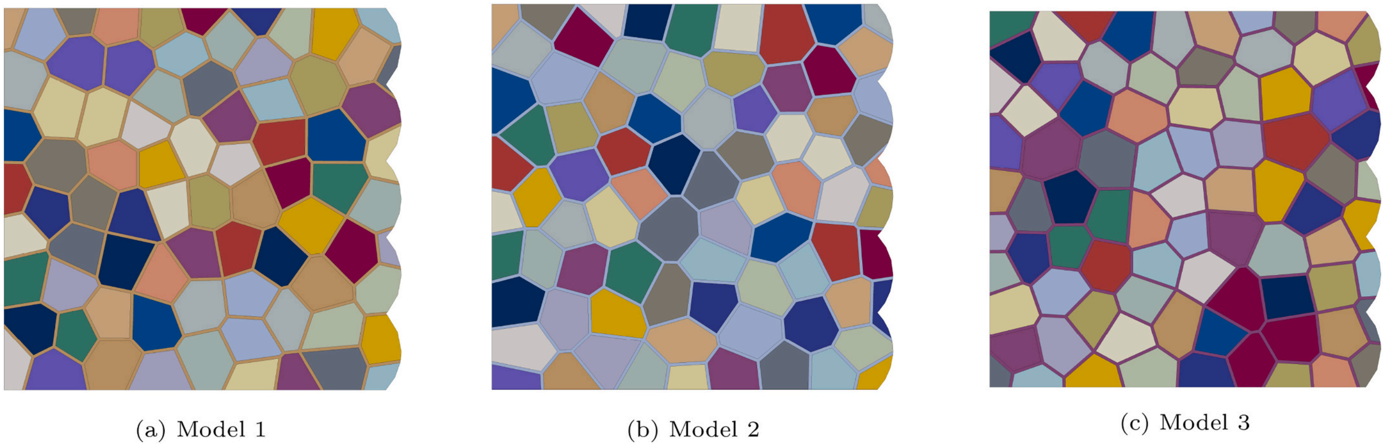
(a) Model 1
(b) Model 2
(c) Model 3

Fig. 43. When the grain size is 500 nm, three grain boundary models are considered.

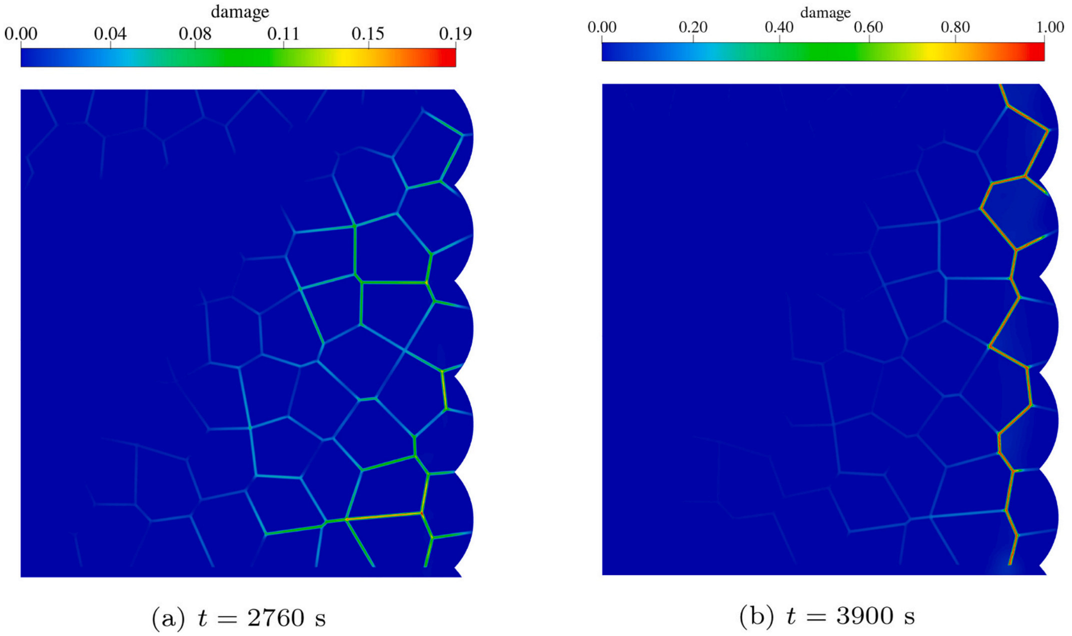

(a) $t = 2760$ s
(b) $t = 3900$ s

Fig. 44. Propagation of cracks within the seed layer.

when the roughness is 0, the initiation time and temperature of cracking are the highest. However, when the roughness is not 0, the interfacial initiation time and temperature decrease first until reaching a certain threshold. After that, as the roughness further increases, the interfacial initiation time and temperature increase again.

6.6. *Interfacial cracking within the seed layer*

Influenced by the fabrication process of the TSV structure, it is necessary to deposit an additional copper seed layer on the barrier layer before the electroplating filling of Cu. Chen et al. [43] discovered that when TSV-Cu bulges, its cracks may propagate along the Cu seed layer. They also found that this crack propagation is closely related to the microstructure of the TSV-Cu seed layer. To investigate the relationship between crack propagation in the seed layer and grain orientation, this section explores the influence pattern by constructing models with different grain orientations within the TSV-Cu seed layer.

Fig. 41a presents a schematic diagram of the copper seed layer. Fig. 41b is a Voronoi polygons model used for numerical calculation. In the TSV, the cracks propagate along the grain boundaries; hence, the model incorporates copper grain boundaries. Additionally, the mesh of the copper grains and grain boundaries is also presented in the Fig. 41b. The mesh size is 0.00001 mm, the crack length scale l_0 is 0.00005 mm, the average grain size is 500 nm, and the thickness of the grain boundary is 40 nm. Its tensile strength is 193 MPa [48], the fracture energy G_C is 3 N/m, and the shear-to-stretch ratio χ is 0.6. The remaining parameters are consistent with those shown in Table 3. Fig. 42 presents the FE model of the TSV blind hole, with the TSV-Cu and Si interface set as fully bonded and the interface roughness at 0.2. Three different models, as shown in Fig. 43, are established to simulate intergranular fracture with cracks propagating in different grain orientations. As shown in Fig. 43a, the model includes 457,432 quadrilateral UEL elements and 457,432 coupled temperature-displacement quadrilateral elements. A global heating rate of 10 °C/min is applied to the model, with a time increment Δt of 0.25 min. The remaining conditions are consistent with those in Table 3.

Fig. 44 shows the crack propagation path of the grain orientation model corresponding to Fig. 43a when the temperature is raised to 485 °C. It can be seen from the figure that the damage within the grain boundary layer mainly occurs at the junctions of the grain boundaries

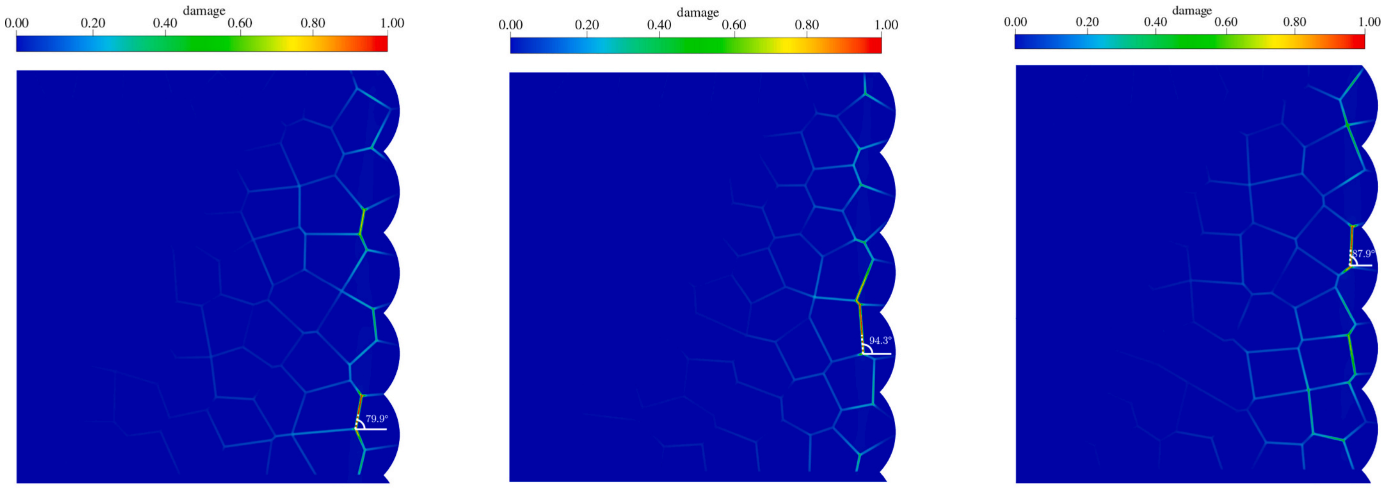

(a) Model 1 (b) Model 2 (c) Model 3

Fig. 45. Crack initiation positions for different grain orientations.

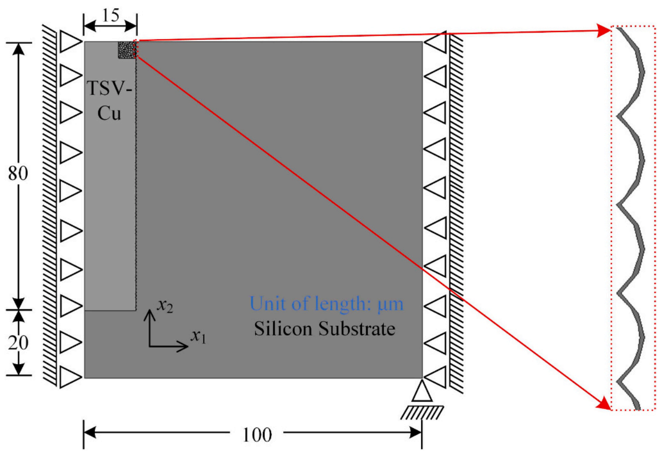

Fig. 46. The structure of the seed layer and interface layer in TSV structures.

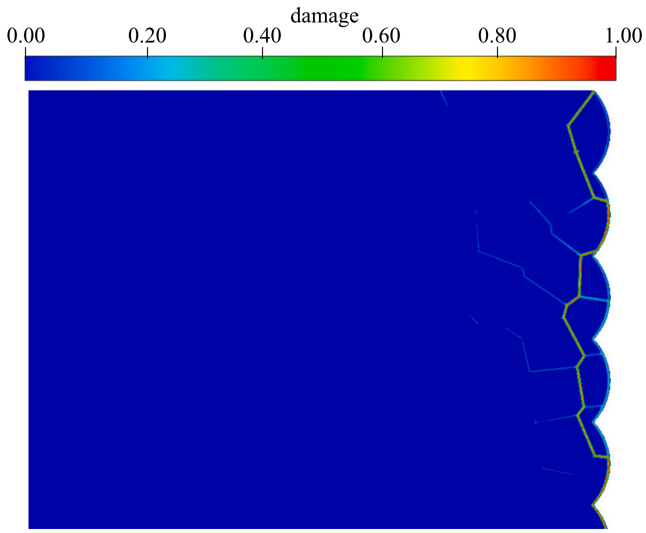

Fig. 47. The propagation of cracks within the seed layer and interface layer.

near the TSV-Cu and Si interface. As the temperature further increases, cracks form near the interface within TSV-Cu (as shown in Fig. 44b), and the cracks tend to propagate along the sidewall grain boundaries. Fig. 45 presents the initial crack positions for the grain orientations in Fig. 43. Comparing the crack initiation positions of the 3 models reveals that the damage occurs closer to the interface. Furthermore, the smaller the axial angle of the grain boundary with the x_2 direction, the more prone it is to crack formation.

6.7. *Crack mixed propagation at the seed layer and TSV interface*

To further investigate the failure modes of TSV structures during thermal annealing, this section utilizes the proposed phase field model to compute the mixed crack propagation behavior occurring at the seed layer and interface layer. Fig. 46 depicts the computational model employed in this section, which extends the model in Fig. 42 by adding a TSV interface layer to simulate the crack propagation. The interface layer thickness and the TSV-Cu grain boundary layer thickness are both 40 nm. The mesh size is 0.00001 mm, and the length scale parameter l_0 is 0.00005 mm. A global heating rate of 10 °C/min is applied to the model, with a time increment of 0.5 min. The tensile strength of the grain boundary layer is 40 MPa, while all other material properties remain consistent with those shown in Sections 6.6. The boundary conditions are consistent with those described in Section 6.6.

The numerical results, as shown in Fig. 47, indicate that the crack propagates from within the seed layer towards the TSV interface layer. Subsequently, it extends back into the seed layer and continues to propagate within the grain boundaries of the seed layer.

7. Conclusions

This work introduces a computational framework for a thermo-mechanically coupled phase-field model that considers mixed-mode fracture, aimed at simulating the mechanical performance and fracture behavior of interconnect structures TSV and TGV in 3D packaging technologies. The proposed thermomechanically coupled phase-field model reduces the sensitivity of computational results to the length scale parameter l_0. The contribution of this research lies in providing a novel method for studying and analyzing the mechanical properties of interconnect structures during manufacturing and usage processes, and further simulating the formation and evolution of cracks due to thermal cycling in interconnect structures. Through the numerical analysis of TGV and TSV, we can draw the following conclusions respectively.

Through the phase-field simulation of the TGV structure, the calculated microcracks at the edges of the RDL closely matched those observed in experiments. Further, by reducing the copper wall thickness of the TGV, the reliability of the structure can be improved. The calculations for TGV-Cu with the same filling volume under different via shapes revealed that among the double-tapered via, vertical via, and single-tapered via, the double-tapered via has the highest reliability, followed by the vertical via, with the single-tapered via being the least reliable. The numerical examples also calculated circumferential and radial cracks formed under cooling and heating loads on the TGV structure, showing that the crack morphology obtained with the proposed phase-field model closely matches experimental observations. Subsequent calculations for TGV models with different via spacings indicated that as the spacing between TGV vias increases, both the initiation time and temperature of the cracks also increase, suggesting that increasing the via spacing can enhance the reliability of the TGV structure.

Through the phase-field calculations for TSV interconnect structures, it was found that when the height (H) of the TSV-Cu is fixed, a higher aspect ratio strengthens the interface layer's resistance to damage, thereby stabilizing the structure; conversely, with a fixed radius (R) in the TSV-Cu, a higher aspect ratio weakens the interface layer's resistance to damage, making the structure more susceptible to failure. The introduction of roughness in TSV holes significantly decreases the interface layer's reliability. However, as roughness further increases, the initiation time and temperature for cracking also increase, yet they remain much lower than in interfaces without roughness. During the calculation of crack evolution in TSV-Cu, models with different grain orientations in TSV-Cu suggest that crack initiation often occurs at grain boundaries with small angles relative to the y-axis. Subsequent calculations of mixed crack propagation occurring at TSV-Cu grain boundaries and the TSV-Cu/Si interface showed that the proposed phase-field model effectively captures the fracture evolution path.

In future work, the authors will incorporate temperature-dependent material parameters and fracture toughness to achieve a more comprehensive understanding of package interconnect structure. While the long-term fatigue effects in these structures during the device's service life were not explored, we acknowledge the importance of this aspect and plan to investigate fatigue-related issues in subsequent research. Additionally, we intend to explore the use of explicit solver algorithms for phase field problems and compare the results and efficiency of implicit versus explicit solvers.

CRediT authorship contribution statement

Yanpeng Gong: Writing – review & editing, Writing – original draft, Supervision, Software, Project administration, Methodology, Formal analysis. **Yuguo Kou:** Software, Visualization. **Qiang Yue:** Supervision. **Xiaoying Zhuang:** Supervision. **Fei Qin:** Supervision. **Qiao Wang:** Supervision. **Timon Rabczuk:** Supervision.

Declaration of competing interest

The authors declare that they have no known competing financial interests or personal relationships that could have appeared to influence the work reported in this paper.

Data availability

Data will be made available on request.

Acknowledgements

The authors acknowledge the support from the National Natural Science Foundation of China (No. 12002009) and the Alexander von Humboldt Foundation, Germany.

References

[1] G.E. Moore, Cramming more components onto integrated circuits, Proc. IEEE 86 (1) (1998) 82–85.

[2] O. Ahmed, G. Jalilvand, S. Pollard, C. Okoro, T. Jiang, The interfacial reliability of through-glass vias for 2.5 D integrated circuits, Microelectron. Int. 37 (4) (2020) 181–188.

[3] R.W. Keyes, Physical limits of silicon transistors and circuits, Rep. Prog. Phys. 68 (12) (2005) 2701.

[4] S.F. Al-Sarawi, D. Abbott, P.D. Franzon, A review of 3-D packaging technology, IEEE Trans. Components Packag. Manuf. Technol. Part B 21 (1) (1998) 2–14.

[5] J.H. Lau, Overview and outlook of through-silicon via (TSV) and 3D integrations, Microelectron. Int. 28 (2) (2011) 8–22.

[6] J.H. Lau, C.-K. Lee, C.-J. Zhan, S.-T. Wu, Y.-L. Chao, M.-J. Dai, R.-M. Tain, H.-C. Chien, J.-F. Hung, C.-H. Chien, et al., Through-silicon hole interposers for 3-D IC integration, IEEE Trans. Compon. Packag. Manuf. Technol. 4 (9) (2014) 1407–1419.

[7] I. De Wolf, K. Croes, O.V. Pedreira, R. Labie, A. Redolfi, M. Van De Peer, K. Vanstreels, C. Okoro, B. Vandevelde, E. Beyne, Cu pumping in TSVs: effect of pre-CMP thermal budget, Microelectron. Reliab. 51 (9–11) (2011) 1856–1859.

[8] C. Okoro, J.W. Lau, F. Golshany, K. Hummler, Y.S. Obeng, A detailed failure analysis examination of the effect of thermal cycling on Cu TSV reliability, IEEE Trans. Electron Dev. 61 (1) (2013) 15–22.

[9] S. Chen, Z. Wang, Y. En, Y. Huang, F. Qin, T. An, The experimental analysis and the mechanical model for the debonding failure of TSV-Cu/Si interface, Microelectron. Reliab. 91 (2018) 52–66.

[10] C. Wu, T. Jiang, J. Im, K.M. Liechti, R. Huang, P.S. Ho, Material characterization and failure analysis of through-silicon vias, in: Proceedings of the 21th International Symposium on the Physical and Failure Analysis of Integrated Circuits (IPFA), IEEE, 2014, pp. 312–316.

[11] C. Okoro, T. Allowatt, S. Pollard, Resolving thermo-mechanically induced circumferential crack formation in copper through-glass vias, in: 2021 IEEE 71st Electronic Components and Technology Conference (ECTC), IEEE, 2021, pp. 954–958.

[12] S.-K. Ryu, K.-H. Lu, X. Zhang, J.-H. Im, P.S. Ho, R. Huang, Impact of near-surface thermal stresses on interfacial reliability of through-silicon vias for 3-D interconnects, IEEE Trans. Device Mater. Reliab. 11 (1) (2010) 35–43.

[13] K. Demir, T. Ogawa, V. Sundaram, P.M. Raj, R.R. Tummala, Reliability of through-package-vias from via-first processing with ultra-thin glass, IEEE Trans. Device Mater. Reliab. 17 (4) (2017) 683–691.

[14] K. Demir, V. Sukumaran, Y. Sato, A. El Amrani, K. Ramachandran, R. Pucha, P. Markondeya Raj, V. Sundaram, R. Tummala, Reliability of fine-pitch through-vias in glass interposers and packages for high-bandwidth computing and communications, J. Mater. Sci. Mater. Electron. 29 (2018) 12669–12680.

[15] J. Zhao, Z. Chen, F. Qin, D. Yu, Thermo-mechanical reliability study of through glass vias in 3D interconnection, Micromachines 13 (10) (2022) 1799.

[16] H. Badnava, M.A. Msekh, E. Etemadi, T. Rabczuk, An h-adaptive thermo-mechanical phase field model for fracture, Finite Elem. Anal. Des. 138 (2018) 31–47.

[17] C. Miehe, F. Welschinger, M. Hofacker, Thermodynamically consistent phase-field models of fracture: variational principles and multi-field FE implementations, Int. J. Numer. Methods Eng. 83 (10) (2010) 1273–1311.

[18] T.K. Mandal, V.P. Nguyen, J.-Y. Wu, C. Nguyen-Thanh, A. de Vaucorbeil, Fracture of thermo-elastic solids: phase-field modeling and new results with an efficient monolithic solver, Comput. Methods Appl. Mech. Eng. 376 (2021) 113648.

[19] J. Fang, C. Wu, T. Rabczuk, C. Wu, C. Ma, G. Sun, Q. Li, Phase field fracture in elasto-plastic solids: Abaqus implementation and case studies, Theor. Appl. Fract. Mech. 103 (2019) 102252.

[20] Y. Su, G. Fu, C. Liu, K. Zhang, L. Zhao, C. Liu, A. Liu, J. Song, Thermo-elasto-plastic phase-field modelling of mechanical behaviours of sintered nano-silver with randomly distributed micro-pores, Comput. Methods Appl. Mech. Eng. 378 (2021) 113729.

[21] C. Miehe, H. Dal, L.-M. Schänzel, A. Raina, A phase-field model for chemo-mechanical induced fracture in lithium-ion battery electrode particles, Int. J. Numer. Methods Eng. 106 (9) (2016) 683–711.

[22] T.-T. Nguyen, D. Waldmann, T.Q. Bui, Computational chemo-thermo-mechanical coupling phase-field model for complex fracture induced by early-age shrinkage and hydration heat in cement-based materials, Comput. Methods Appl. Mech. Eng. 348 (2019) 1–28.

[23] J.-Y. Wu, W.-X. Chen, Phase-field modeling of electromechanical fracture in piezoelectric solids: analytical results and numerical simulations, Comput. Methods Appl. Mech. Eng. 387 (2021) 114125.

[24] J. Choo, W. Sun, Cracking and damage from crystallization in pores: coupled chemo-hydro-mechanics and phase-field modeling, Comput. Methods Appl. Mech. Eng. 335 (2018) 347–379.

[25] Z.A. Wilson, C.M. Landis, Phase-field modeling of hydraulic fracture, J. Mech. Phys. Solids 96 (2016) 264–290.

[26] P. Li, D. Li, Q. Wang, K. Zhou, Phase-field modeling of hydro-thermally induced fracture in thermo-poroelastic media, Eng. Fract. Mech. 254 (2021) 107887.

[27] P. Li, W. Li, B. Li, S. Yang, Y. Shen, Q. Wang, K. Zhou, A review on phase field models for fracture and fatigue, Eng. Fract. Mech. 289 (2023) 109419.

[28] J.-Y. Wu, A unified phase-field theory for the mechanics of damage and quasi-brittle failure, J. Mech. Phys. Solids 103 (2017) 72–99.

[29] Q. Wang, Y. Feng, W. Zhou, Y. Cheng, G. Ma, A phase-field model for mixed-mode fracture based on a unified tensile fracture criterion, Comput. Methods Appl. Mech. Eng. 370 (2020) 113270.

[30] H. Wang, P. Cheng, S. Wang, H. Wang, T. Gu, J. Li, X. Gu, G. Ding, Effect of thermal treatment on the mechanical properties of cu specimen fabricated using electrodeposition bath for through-silicon-via filling, Microelectron. Eng. 114 (2014) 85–90.

[31] Q. Wang, W. Zhou, Y. Feng, The phase-field model with an auto-calibrated degradation function based on general softening laws for cohesive fracture, Appl. Math. Model. 86 (2020) 185–206.

[32] M. Ambati, T. Gerasimov, L. De Lorenzis, A review on phase-field models of brittle fracture and a new fast hybrid formulation, Comput. Mech. 55 (2) (2015) 383–405.

[33] E. Tanné, T. Li, B. Bourdin, J.-J. Marigo, C. Maurini, Crack nucleation in variational phase-field models of brittle fracture, J. Mech. Phys. Solids 110 (2018) 80–99.

[34] J.-Y. Wu, V.P. Nguyen, A length scale insensitive phase-field damage model for brittle fracture, J. Mech. Phys. Solids 119 (2018) 20–42.

[35] G. Liu, Q. Li, M.A. Msekh, Z. Zuo, Abaqus implementation of monolithic and staggered schemes for quasi-static and dynamic fracture phase-field model, Comput. Mater. Sci. 121 (2016) 35–47.

[36] X. Hu, S. Tan, D. Xia, L. Min, H. Xu, W. Yao, Z. Sun, P. Zhang, T. Quoc Bui, X. Zhuang, T. Rabczuk, An overview of implicit and explicit phase field models for quasi-static failure processes, implementation and computational efficiency, Theor. Appl. Fract. Mech. 124 (2023) 103779.

[37] E. Qin, L. Lu, N. Tao, J. Tan, K. Lu, Enhanced fracture toughness and strength in bulk nanocrystalline Cu with nanoscale twin bundles, Acta Mater. 57 (20) (2009) 6215–6225.

[38] D.S. Cronin, K. Bui, C. Kaufmann, G.J. McIntosh, T. Berstad, Implementation and Validation of the Johnson-Holmquist Ceramic Material Model in LS-Dyna. 4th European LS-DYNA Users Conference, 2003, pp. 47–60.

[39] J. Zhao, Z. Chen, F. Qin, D. Yu, Thermo-mechanical reliability study of through glass vias in 3D interconnection, Micromachines 13 (10) (2022).

[40] C. Okoro, T. Allowatt, S. Pollard, Resolving thermo-mechanically induced circumferential crack formation in copper through-glass vias, in: 2021 IEEE 71st Electronic Components and Technology Conference (ECTC), 2021, pp. 954–958.

[41] C. Okoro, S. Jayaraman, S. Pollard, Understanding and eliminating thermo-mechanically induced radial cracks in fully metallized through-glass via (TGV) substrates, Microelectron. Reliab. 120 (2021) 114092.

[42] X. Liu, Q. Chen, P. Dixit, R. Chatterjee, R.R. Tummala, S.K. Sitaraman, Failure mechanisms and optimum design for electroplated copper Through-Silicon Vias (TSV), in: 2009 59th Electronic Components and Technology Conference, 2009, pp. 624–629.

[43] S. Chen, F. Qin, T. An, P. Chen, B. Xie, X. Shi, Protrusion of electroplated copper filled in through silicon vias during annealing process, Microelectron. Reliab. 63 (2016) 183–193.

[44] P. Skalka, M. Kotoul, Determination of mechanical and fracture properties of silicon single crystal from indentation experiments and finite element modelling, Materials 14 (22) (2021).

[45] S. Uehara, K. Ito, K. Kohama, T. Onishi, Y. Shirai, M. Murakami, Resistivity reduction and adhesion increase induced by surface and interface segregation of Ti atoms in Cu(Ti) alloy films on glass substrates, Mater. Trans. 51 (2010) 1627–1632.

[46] C. Wu, T. Jiang, J. Im, K.M. Liechti, R. Huang, P.S. Ho, Material characterization and failure analysis of through-silicon vias, in: Proceedings of the 21th International Symposium on the Physical and Failure Analysis of Integrated Circuits (IPFA), 2014, pp. 312–316.

[47] N. Ranganathan, K. Prasad, N. Balasubramanian, K.L. Pey, A study of thermo-mechanical stress and its impact on through-silicon vias, J. Micromech. Microeng. 18 (7) (2008) 075018.

[48] S. Zhang, M. Sakane, T. Nagasawa, K. Kobayashi, Mechanical properties of copper thin films used in electronic devices, Procedia Eng. 10 (2011) 1497–1502, 11th International Conference on the Mechanical Behavior of Materials (ICM11).